SANDIA REPORT
SAND2010-6412
Unlimited Release
Printed October 2010

METHODS FOR MODELING IMPACT-INDUCED REACTIVITY CHANGES IN SMALL REACTORS

Jeffery A. Smith, Daniel L. Villa, Brandon M. Smith, Ross F. Radel, Tracy E. Radel, Tyler N. Tallman, Ronald J. Lipinski, and Paul P. H. Wilson

Prepared by
Sandia National Laboratories
Albuquerque, New Mexico 87185 and Livermore, California 94550

Sandia National Laboratories is a multi-program laboratory managed and operated by Sandia Corporation, a wholly owned subsidiary of Lockheed Martin Corporation, for the U.S. Department of Energy's National Nuclear Security Administration under contract DE-AC04-94AL85000.

Approved for public release, further dissemination unlimited.

Sandia National Laboratories

Issued by Sandia National Laboratories, operated for the United States Department of Energy by Sandia Corporation.

NOTICE: This report was prepared as an account of work sponsored by an agency of the United States Government. Neither the United States Government, nor any agency thereof, nor any of their employees, nor any of their contractors, subcontractors, or their employees, make any warranty, express or implied, or assume any legal liability or responsibility for the accuracy, completeness, or usefulness of any information, apparatus, product, or process disclosed, or represent that its use would not infringe privately owned rights. Reference herein to any specific commercial product, process, or service by trade name, trademark, manufacturer, or otherwise, does not necessarily constitute or imply its endorsement, recommendation, or favoring by the United States Government, any agency thereof, or any of their contractors or subcontractors. The views and opinions expressed herein do not necessarily state or reflect those of the United States Government, any agency thereof, or any of their contractors.

Printed in the United States of America. This report has been reproduced directly from the best available copy.

Available to DOE and DOE contractors from
U.S. Department of Energy
Office of Scientific and Technical Information
P.O. Box 62
Oak Ridge, TN 37831

Telephone: (865)576-8401
Facsimile: (865)576-5728
E-Mail: reports@adonis.osti.gov
Online ordering: http://www.osti.gov/bridge

Available to the public from
U.S. Department of Commerce
National Technical Information Service
5285 Port Royal Rd
Springfield, VA 22161

Telephone: (800)553-6847
Facsimile: (703)605-6900
E-Mail: orders@ntis.fedworld.gov
Online order: http://www.ntis.gov/help/ordermethods.asp?loc=7-4-0#online

SAND2010-6412
Unlimited Release
Printed October 2010

METHODS FOR MODELING IMPACT-INDUCED REACTIVITY CHANGES IN SMALL REACTORS

Jeffery A. Smith, Daniel L. Villa, Ross F. Radel, Tracy E. Radel,
Tyler N. Tallman and Ronald J. Lipinski
P. O. Box 5800
Sandia National Laboratories, Albuquerque, NM 87185

Brandon M. Smith and Paul P. H. Wilson
U. of Wisconsin, Madison, WI

Abstract

This paper describes techniques for determining impact deformation and the subsequent reactivity change for a space reactor impacting the ground following a potential launch accident or for large fuel bundles in a shipping container following an accident. This technique could be used to determine the margin of subcriticality for such potential accidents. Specifically, the approach couples a finite element continuum mechanics model (Pronto3D or Presto) with a neutronics code (MCNP). DAGMC, developed at the University of Wisconsin-Madison, is used to enable MCNP geometric queries to be performed using Pronto3D output. This paper summarizes what has been done historically for reactor launch analysis, describes the impact criticality analysis methodology, and presents preliminary results using representative reactor designs.

Acknowledgments

The authors wish to thank Dana Powers and John E. Kelly for their steadfast support of this work. This LDRD Project (130753) was supported by Laboratory Directed Research and Development, Sandia National Laboratories. Sandia is a multiprogram laboratory operated by Sandia Corporation, a Lockheed Martin Company, for the United States Department of Energy's National Nuclear Security Administration under Contract DE-AC04-94AL85000.

Table of Contents

1. Introduction 9
2. Previous work 11
3. Potential Impact Conditions 15
4. Representative Reactor Design 17
5. Impact Mechanical Modeling 19
    5.1. Initial Test Cases 19
        5.1.1. Simple Cylinder 19
        5.1.2. Scaled Down Full Reactor Model (19 pins) 20
    5.2. Geometry and Meshing 23
    5.3. Material Properties 26
    5.4. Computational Details 32
    5.5. Impact Results 37
    5.6. Future capabilities 41
    5.7. Impact Modeling Conclusions 41
6. Preliminary Impact Reactivity Modeling 43
    6.1. Zero Order Modeling of Impact Reactivity Change 43
        6.1.1. 19-pin Rector Studies 43
    6.2. Simple Cylinder Modeling with DAGMC 47
7. Advanced Impact Modeling with DAGMC 49
    7.1. Introduction to DAG-MCNP5 49
        7.1.1. Unique Challenges of Deformed Geometry 49
        7.1.2. Deformed Geometry Workflow 50
    7.2. Geometry Initialization 50
    7.3. Particle Transport 52
        7.3.1. Geometric Model 52
        7.3.2. Point Membership Test 53
        7.3.3. Tracking Algorithm 56
    7.4. Reactivity Calculations 59
        7.4.1. Incremental Development 59
        7.4.2. Comparison of Native and CAD Geometry 60
        7.4.3. 85-Pin Reactor Impact Simulations 61
    7.5. Future Work 67
8. Summary and Conclusions 69
9. References 71

List of Figures

Figure 3-1. Impact Velocity vs. Initial Altitude. 16
Figure 4-1. 3-D Cutaway View of the Baseline 85-Pin Reactor. 17
Figure 4-2. Cross Sections of Baseline Design Reactor Core. 18
Figure 5-1. Initial Test Geometry. 19
Figure 5-2. Geometry of 19-Pin Reactor FEA Model. 21
Figure 5-3. Meshed Detail of 19-Pin Reactor FEA Model. 21
Figure 5-4. Resulting Deformed Geometry of Portion of 19-Pin Reactor Modeled in the FEA. 22
Figure 5-5. Resulting Deformed Shape of Fuel in the 19-Pin Reactor. 22
Figure 5-6 Horizontal Cross Section of Geometry from Top. 24
Figure 5-7 Detailed View of Nuclear Fuel Cross Section. 25
Figure 5-8. Vertical Cross Section of Geometry. 25
Figure 5-9 NAK Flow Illustration and Other Details. 26
Figure 5-10. SPH Overlap Illustration. 26
Figure 5-11. Stress-Strain Curves for Beryllium and SS316. 28
Figure 5-12 Concrete tensile damage function. 29
Figure 5-13. Dynamic Increase Factor vs. Strain Rate. 30
Figure 5-14. Concrete pressure and bulk modulus vs. volumetric strain functions. 31
Figure 5-15 1/12th symmetry model Cuts in UO2 Fuel. 32
Figure 5-16. ½ Symmetry Model, Collision Angle Convention and View of Cuts in the Fuel Pins. 33
Figure 5-17. Procedure to Communicate with DAGMC. 34
Figure 18 Zero Degree Collision with and without SPH Elements. 38
Figure 19 Strain at Center Pin. 38
Figure 20. Advancing NAK Jet. 39
Figure 21 Final Time Calculated for 45 Degree No-SPH Simulation. 40
Figure 22. Hourglass Aggravated Surface Due to High Pressure SPH Contact Interactions. 40
Figure 6-1. 19-pin Reactor Configuration. 44
Figure 6-2. Top View of 19-Pin Reactor Cross Section. 44
Figure 6-3. Lower Portion Fuel Geometry in 19-Pin Post-Impact Approximated Geometry. 45
Figure 6-4. Front Cross-Sectional View of 19-Pin Post-Impact Approximated Geometry. 46
Figure 6-5. Top Cross-Sectional View of 85-Pin, Pre-Impact Geometry. 47
Figure 7-1. Undeformed Cubit Mesh (a) and DAGMC Geometry at 0.225 ms (b). 51
Figure 7-2. 2-D Volume before (a) and after (b) Impact. 52
Figure 7-3. Enlarged Orientation (a) and Ray Crossing (b) Methods. 54
Figure 7-4. Deformed Structural Component (a) and Surrounding Fluid (b) Volumes Decomposed into 2-Manifolds. 54
Figure 7-5. Particle Track through a Volume Containing an Overlap. 57
Figure 7-6. Native MCNP (a,b) and Converted CAD Geometry (c). 60
Figure 7-7. 0-degree Impact at 0 ms (a) and 1.5 ms (b). 62
Figure 7-8. Node Displacement and Number of Dead Elements during 0-Degree Impact. 62
Figure 7-9. Neutron Multiplication Factor during 0-Degree Impact. 63
Figure 7-10. 0-Degree Impact at 1.5 ms without (a) and with (b) SPH Elements. 64
Figure 7-11. Node Displacement and Number of Dead Elements during 0-degree Impact, with SPH Elements in Structural Simulation. 64

Figure 7-12. Neutron Multiplication Factor during 0-Degree Impact, with SPH Elements in the Structural Simulation. 65
Figure 7-13. 45-Degree Impact at 0 ms (a) and 2.1 ms (b). 66
Figure 7-14. Node Displacement and Number of Dead Elements during 45-Degree Impact. 66
Figure 7-15. Neutron Multiplication Factor during 45-Degree Impact. 67

List of Tables

Table 4-1. Reactor Design Parameters. 18
Table 5-1. Material Constants Used. 27
Table 5-2. Death Criteria Used. 27
Table 5-3 Multilinear Stress Strain Curves for SS316 and Be. 28
Table 5-4. Additional Concrete Parameters. 29
Table 5-5. Damage Function and Dynamic Increase Factor Function for Concrete. 29
Table 5-6. Concrete Pressure and Bulk Modulus Functions. 30
Table 5-7. Fluid Properties. 31
Table 5-8. UO_2 Soil and Foam Properties. 31
Table 6-1. Design Parameters for the 19-Pin Concept. 43
Table 6-2. MCNP Results for 19-pin Reactor Model. 46
Table 6-3. MCNP Results for 85-pin Reactor Model 47
Table 6-4. Results of Test Problem using Different MCNP5 Geometry Representations. 48
Table 7-1. Results of Point Membership Test 53
Table 7-2. Surface Crossing Parity of 2-Manifolds. 55
Table 7-3. Summary of Models Used for Development of Workflow and Tracking Algorithm. 60
Table 7-4. Results of 85-pin Comparison between Native MCNP5 and New Version of DAG-MCNP5. 60
Table 7-5. Summary of 85-Pin Reactor Impact Models. 61

Acronyms and Abbreviations

ASRG	Advanced Stirling Radioisotope Generator
BCI	Bare Clad Impact
DAGMC	Direct Accelerated Geometry, Monte Carlo
DOE	Department of Energy
FC	Fueled Clad
FPT	Flyer Plate Test
FWPF	Fine-Weave Pierced-Fabric
GIS	Graphite Impact Shells
GPHS	General Purpose Heat Source
INSRP	Interagency Nuclear Safety Review Panel
MCNP	Monte Carlo N-Particle
MMRTG	Multi-mission Radioisotope Thermoelectric Generator
MOAB	Mesh Oriented datABase
MSL	Mars Science Lab
NASA	National Aeronautics and Space Administration
OBB	Oriented Bounding Box
PNH	Pluto New Horizons
PuO_2	Plutonium dioxide
RTG	Radioisotope Thermoelectric Generator
RPS	Radioisotope Power Source
SNL	Sandia National Laboratories
SPF	Solid Propellant Fire
SPH	Smoothed Particle Hydrodynamics
SRB	Solid Rocket Booster
SVT	Safety Verification Test
UO_2	Uranium dioxide

1. INTRODUCTION

D. L. Villa and R. J. Lipinski

Assessing the change in reactivity of nuclear reactors or nuclear fuel assemblies for deformed configurations during impact events is an undeveloped area of nuclear safety analysis.[1] Examples of possible applications of such a capability include safety analysis for launch of a small space reactor or analysis of nuclear fuel in shipping containers under very severe impacts. Sandia National Laboratories (SNL) and the University of Wisconsin (UWISC) have worked together to build such a capability through expanding a software named, "Direct Accelerated Geometry Monte Carlo" (DAGMC) [Tautges 2009] which can take the time-dependent impacted geometry from Sandia's continuum mechanics codes Pronto3D [Attaway 2000a]] and Presto [Sierra 2010] and calculate a time dependent criticality of the assembly.

This report provides an in-depth look at the techniques needed to model reactor or bundle deformation during an impact and the resulting change in reactivity. The baseline chosen for this exploration and demonstration is a conceptual design for a small eighty-five pin space reactor that impacts the ground following a postulated launch accident. These efforts serve as a demonstration that such modeling is within the capability of present day computers. The results also show that there can be significant variations in reactivity due to deformations, depending on the impact conditions and the reactor configuration. The developments presented are the continuation of the work presented by Radel, et al. [Radel 2009].

The change in reactivity for a nuclear reactor or fuel bundle resulting from an impact is difficult to model accurately. Achieving the sensitivity needed requires fluid-structure interactions for large deformations, intricate geometry for flow paths, and accurate material properties. These requirements drive multiple issues which will need to be addressed in future experimental and computational research and development. Part of the solution to modeling the impact deformation accurately is having a continuum mechanics code that can handle large deformations and even cracking and tearing of materials. Sandia's Pronto3d and Presto codes are the latest in a series of developmental efforts by Sandia in modeling the large deformation and fracturing of extended objects undergoing impact. They incorporate the latest numerical techniques from decades of continuum mechanics modeling as well as the experience gained from numerous impact tests [Gwinn 2004]. The other part of the solution is having material models that reflect the material behavior at large deformations and at appropriately high strain rates.

Uranium dioxide (UO_2) is the dominant fuel type for most reactors. It can have a wide range in performance based on the history and processing involved. Crushing or distortion of the fuel is a potential outcome for impact events, but the extent and nature of the energy dissipated in such events is not well determined. The approach used in the modeling for this project is described in some detail in Chapter 5 of this report.

---

[1] Reactivity is a measure of the nearness to a self-sustaining nuclear chain reaction. A reactor with a sustained chain reaction in which the power is neither decreasing nor increasing has a reactivity of zero and has achieved criticality. If the power is increasing, the reactivity is positive. If the power is decreasing, the reactivity is negative and the reactor is sub-critical.

Liquid-metal sodium potassium (NaK) is a coolant that has been used in past reactors and proposed for future space reactors. It can potentially cushion the nuclear fuel from some of the impact. Capturing its flow and cushioning behavior requires a fluid-structure interaction which cannot be met by Lagrangian finite element formulations. No constitutive model exists within Presto which would capture its dynamic fluid properties and the correct data was not found. A smoothed particle hydrodynamics (SPH) approach [Swegle 1994] offers the needed flow deformation capability, but calibration of this method to the behavior of NaK would require some work. This approach is also described in Chapter 5 of this report.

Another reason the geometry typical for small reactors or fuel bundles is difficult to model is because many thin sections of stainless steel are present. These sections would usually be represented as shells but have to be solid for the current criticality assessment methods. As a result, all of the geometry must be represented by single point integration hexahedra which require a minimum of three elements through the thickness. The NaK flow paths have details which greatly increases the required size of the model. These small pathways and the NaK properties determine the viscous resistance which will be experienced during an impact.

Once the deformed geometry of the reactor or fuel bundle has been modeled mechanically, there is still a substantial challenge in determining the resulting change in reactivity. Existing nuclear criticality codes are designed to accept simple geometric descriptions as their inputs. The continuously deformed post-impact geometries can only be approximated by hand for these codes. As part of this project a method for handling the continuously deformed geometry in a criticality code was developed. In addition, an automated method for exporting the time-dependent state of deformation and determining the time-dependent reactivity was developed. This is described in Chapter 7 of this report.

It should be noted that the examples shown in this report are meant primarily to demonstrate the techniques developed for modeling impact reactivity and to show the state of the art in that capability, along with its limitations. The particular results obtained are very sensitive to the reactor or fuel bundle design, the assumed impact conditions, as well as the material properties assumed. The material properties in particular need considerable improvement over those assumed in this study. Hence, these results should not be viewed as a definitive answer as to how much reactivity will change for a given accident, but rather as an indication of the potential scale of the effect. Ultimately, improved material properties will be needed to provide better fidelity, and sensitivity studies will be needed to bound the effects of known errors.

2. PREVIOUS WORK

R. J. Lipinski

Significant research has gone into space reactor designs for various programs. Calculations have been performed to demonstrate criticality safety both on Earth and while in orbit. Since the radiological inventory of a nuclear reactor is very small prior to initial operation, the approach has been to demonstrate that the reactor does not become critical and generate radioactive fission products during a launch accident. Past analyses have primarily involved criticality calculations for reactors immersed in water, wet sand or other materials, but without distortion of the initial geometry. Part of the reason for this is the difficulty in calculating the amount of reactor core distortion caused by an accident, as well as the difficulty in determining the reactivity of the distorted geometry.

The only launch of a nuclear reactor into space by the U.S. was SNAP-10A, which was launched on April 3, 1965 [Wilson 1965]. Four hours after launch, reactor startup was initiated and full power (600 We) was achieved nine hours after startup. It operated smoothly for 43 days until a spacecraft electronic fault caused an automatic and permanent shutdown. Since then there have been numerous concepts for space reactors developed to various levels of detail by the U.S., but none have been built or launched into space.

The SP-100 program developed a fairly detailed concept for a 100 kilowatt electric (kWe) reactor power system based on a lithium-cooled uranium nitride (UN) fueled fast reactor and SiGe thermoelectric power conversion [Truscello 1992]. The program also developed and tested some key hardware, including the UN fuel pellets, control drive motors, and prototype heat exchangers. The program was canceled before a reactor could be constructed.

The Jupiter Icy Moons Orbiter (JIMO) program and the subsequent Prometheus program developed several top-level concepts for multi-hundred kWe reactor power systems [Ashcroft 2007]. The dominant options for the reactor were lithium cooled, heatpipe cooled and He/Xe cooled. Sodium, NaK, and water cooled systems were also considered. Power conversion options included thermoelectric, Stirling and Brayton conversion. The level of detail achieved for these concepts was not as great as for the SP-100 program when the Prometheus program was canceled.

More recently NASA has been considering fission surface power systems for a lunar base [Marcille 2006, Poston 2008, Poston 2009] NaK cooled reactor concepts with Stirling power conversion have been reported as the reference concept. Prior to this, NASA and others had considered small reactors for Mars and other missions [Elliott 2003, Lipinski 2002]

In addition to the nuclear electric power systems described above, the U.S. has developed concepts and hardware for nuclear thermal propulsion systems. The Rover/NERVA project produced fairly detailed designs and operating hardware that concluded with several ground tests of a thrusting reactor/rocket that heated hydrogen in the reactor core to develop thrust [Klein 2004, Dewar 2007]. The program culminated with the Pewee reactor thrusting for a total of 40 minutes at full power, including two restarts. Calculations were performed to assess the criticality increase from a postulated reactor impact during a launch accident. An experiment

with a reactor was performed with a reactivity increase rate comparable to the projected rate from a strong impact to help estimate the energy release in such an event [Klein 2004, Dewar 2007]

The Space Nuclear Thermal Propulsion (SNTP) program developed nuclear thermal reactor concepts using particle fuel [Parma 1993]. It produced a fairly high-fidelity criticality experiment and culminated with element testing driven by an external reactor. Neither the Rover/NERVA program nor the SNTP program resulted in launch of a reactor.

For all the programs described above, safety of the system during launch and subsequent operation was always a key consideration in the design process. Particular attention was given to accidents that might occur during the launch process. All of the concepts used highly enriched uranium and it was recognized that prior to operation the radiological inventory of the reactor is very low (typically less than 10 Ci (3.7×10^{11} Bq)). Such a low level of activity would have extremely low health and environmental consequences if there were a launch accident that dispersed the reactor material.

To take advantage of the very low levels of radioactivity in a fresh space reactor, a common approach to safety in these past programs was to avoid operation of the reactor prior to launch and achieving a stable deployment (e.g. on the Moon), trajectory, or orbit. In addition, the reactor would be launched in a substantially subcritical state. Finally, the reactor designs considered environments that might increase the reactivity during a launch accident and materials and geometries were developed to minimize or overcome these potential reactivity increases.

The most commonly addressed source of potential reactivity increase was the submersion of the reactor in water or wet sand near the launch pad. Space reactor concepts use highly enriched uranium to reduce the total system mass needed to achieve criticality, but this leads to the potential that water could moderate the neutrons and increase reactivity. One solution to this issue is a spectral-shifting neutron absorber [King 2004, King 2005]. A spectral-shifting absorber (e.g. Gd or Eu) does not absorb fast neutrons very effectively, but does absorb thermal neutrons fairly readily. This counters the increase in fission cross section as the neutrons are thermalized by water. Another solution is the use of an external neutron reflector that is better at reflection than water or sand (e.g. Be or BeO). Replacement of the reflector by water results in a net decrease in reflection and compensates for the increase in fission cross section.

In most of the past analyses the effect of the water, wet sand, and other accident environments was assessed without formally addressing the potential for deformations due to the accident. Part of the reason for this may have been the difficulty in performing impact calculations. However, the development of finite element continuum mechanics codes and parallel processing computers has reached the point where such calculations are becoming feasible. This paper presents a methodology for performing impact calculations, and mapping the results into a neutron criticality code. It also presents some preliminary results for representative reactor configurations to give some insights on the margins that might be available against impact criticality.

The Monte Carlo Neutron Photon (MCNP) code [Breismeister 1997] is a versatile code for calculating the amount of reactivity of a reactor or fuel bundle. The normal input for this code includes a description of the geometry which is based on assembling portions of cylinders, blocks, spheres, cones, and other simple geometries. Several research groups have developed codes which can take the output of standard computer aided design (CAD) software and produce input files for MCNP. Wu and Xu [Wu 2007] present an overview of some of the methods being developed. They include Visual Editor [Schwartz 2005], MORITZ [White Rock 2010], CAD-MCNPX [Wang 2005], JAEA code [Sato 2006], MC-CAD [Tsiege-Tamirat 2005], TopAct [Raytheon 2010], and RPI code [Caracappa 2005]. However, these codes are suitable only for the simplified geometry of a reactor before distortion by impact. After impact, the geometry is no longer easily described by a small number of cylinders, blocks, spheres, etc. Rather, the geometry needs a very large number of small elements (e.g. blocks or tetrahedrons) to describe it. Because of the large number of elements needed, the problem is intractable computationally using the CAD transfer tools.

The University of Wisconsin has developed a different approach [Tautges 2009, Sawan 2008]. It focuses on modeling just the boundaries between separate material regions. This is an appropriate approach since MCNP tracks the particle trajectories within a material and only needs to interject geometry information as it passes through the boundary between materials. The code being developed for this is called DAGMC. It had been developed to the point of being able to model fairly intricate geometries (e.g. for tokamak fusion reactors). For this LDRD project the capability was expanded considerably to handle the time dependent and intricate distortions of an impact simulation.

3. POTENTIAL IMPACT CONDITIONS

R. J. Lipinski

Potential launch accident scenarios that might lead to distortion of the reactor geometry include blast and impact. Blast effects from liquid propellant are typically much lower than the effects of impact onto the ground. The amount of potential distortion to a reactor during impact is a function of the reactor geometry, the impact velocity and the impacted surface. For purposes of development of the methodology, a representative set of conditions was chosen for the impact and the reactivity calculations.

Typical surfaces that a spacecraft or reactor might impact during a launch accident are concrete, steel, asphalt and sand. The impact velocity depends on the spacecraft or reactor height at the time of the accident, the mass of the system, its cross-sectional area and its drag coefficient. The velocity at impact for an object dropped from an initial altitude of y, including the effects of turbulent air drag, is approximately [French 1971]

$$v = v_t \tanh\left(\frac{gt}{v_t}\right) \tag{3-1}$$

where v_t is the terminal velocity of the object, g is gravitational acceleration (9.81 m/s^2), t is the time it takes for the descent, and tanh is the hyperbolic tangent. The terminal velocity is given by

$$v_t = \sqrt{\frac{2mg}{\rho A C_d}} \tag{3-2}$$

where m is the object's mass, ρ is air density, A is the average cross sectional area during descent perpendicular to the direction of travel, and C_d is the drag coefficient. For a blunt object, a typical drag coefficient is 1. The time it takes for descent is

$$t = \frac{v_t}{g} a\cosh\left(\exp\left(\frac{gy}{v_t^2}\right)\right) \tag{3-3}$$

where acosh is the inverse hyperbolic cosine.

For reference, the height of a payload on an Atlas V launch vehicle above the concrete and steel launch pad is about 50 m, and for the proposed Ares V launch vehicle it is about 100 m. The terminal velocity for the proposed lunar lander (about 45,000 kg, fully loaded, with a diameter of 8 m) is about 120 m/s. The terminal velocity for the reactor power system described by Marcille [Marcille 2006] (1900 kg with water shield, no attached radiator and a diameter of 0.83 m) is about 240 m/s if falling core first. However, it takes a large initial height to achieve 240 m/s, and the launch vehicle could be over sand by that time.

Figure 3-1 shows the impact velocity for the lunar lander and the reactor described above as a function of initial altitude. The launch vehicle will move upward for only a few seconds and then start heading over sand toward the ocean. The maximum impact velocity on the concrete pad is expected to be about 100 m/s.

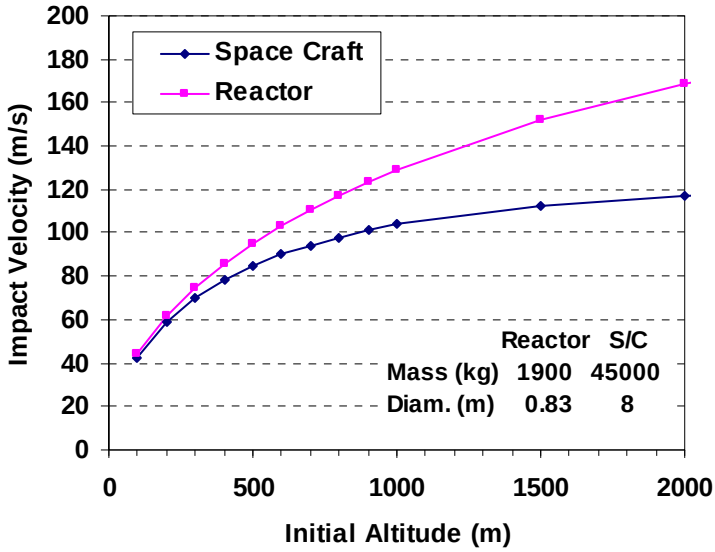

Figure 3-1. Impact Velocity vs. Initial Altitude.

The material surrounding the reactor following impact is a function of the initial configuration and other environmental factors. Usually water or wet sand is assumed so as to give the greatest effect on enhancing reactivity (to yield a conservative calculation). It may be difficult to envision a reactor ending in water following impact on concrete. But there may be the potential to bounce into a nearby flame pit or depression where water spray from the acoustic suppression system might have accumulated. So water will be assumed as one possible medium that could surround the reactor. For scoping purposes, other potential materials for consideration are air, spacecraft debris, wet sand, liquid oxygen and liquid hydrogen (both undergoing film boiling on the surfaces of the reactor vessel).

4. REPRESENTATIVE REACTOR DESIGN

R. F. Radel

The reactor concept reported by Marcille [Marcille 2006] was selected as a baseline design to use for testing the methodologies for impact and reactivity calculation. The 25 kWe reactor described in the Marcille paper is a liquid metal (NaK) cooled, UO_2 fueled, stainless steel clad fast reactor. An isometric view of a CAD model of this reactor is shown in Figure 4-1, and a cross-sectional view of an MCNP model of the reactor is shown in Figure 4-2. The core is composed of 85 UO_2 fuel pins that are enriched to 93% U-235, and are clad in SS316. The NaK coolant is pumped into the core region via a downcomer, is heated by the fuel pins, and is sent to the power conversion system. The power conversion system was not modeled for this study.

The core basket sits within an annular radial beryllium reflector. Six externally driven control drums are located within this reflector region, and are used to control reactivity. The control drums are primarily composed of beryllium. However, the thin crescent-shaped control elements are composed of B_4C. The elements of the drums are shown in a "full in" (shut down) orientation in Figure 4-2. The reactor would be launched in this shut down configuration, and all of the impact studies described in this paper were performed in this configuration. The reactor utilizes a borated water radial shield contained in a SS vessel, and a thicker borated water shield on the top (not shown). Various design parameters are listed in Table 4-1.

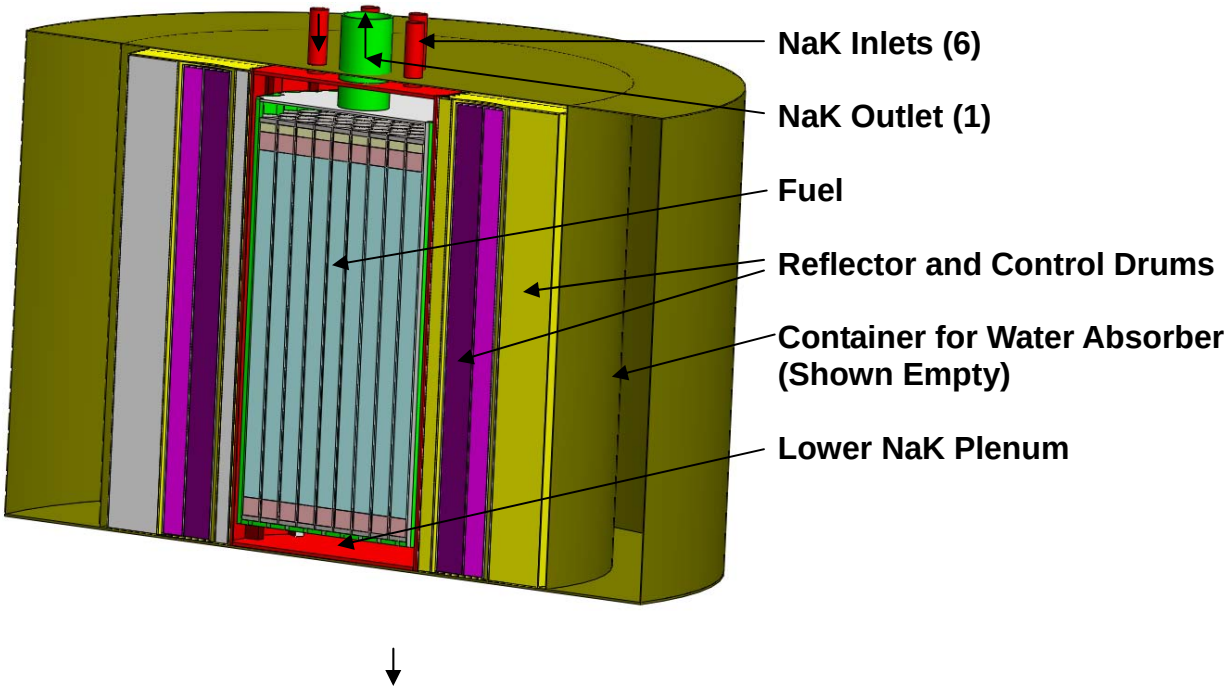

Figure 4-1. 3-D Cutaway View of the Baseline 85-Pin Reactor.

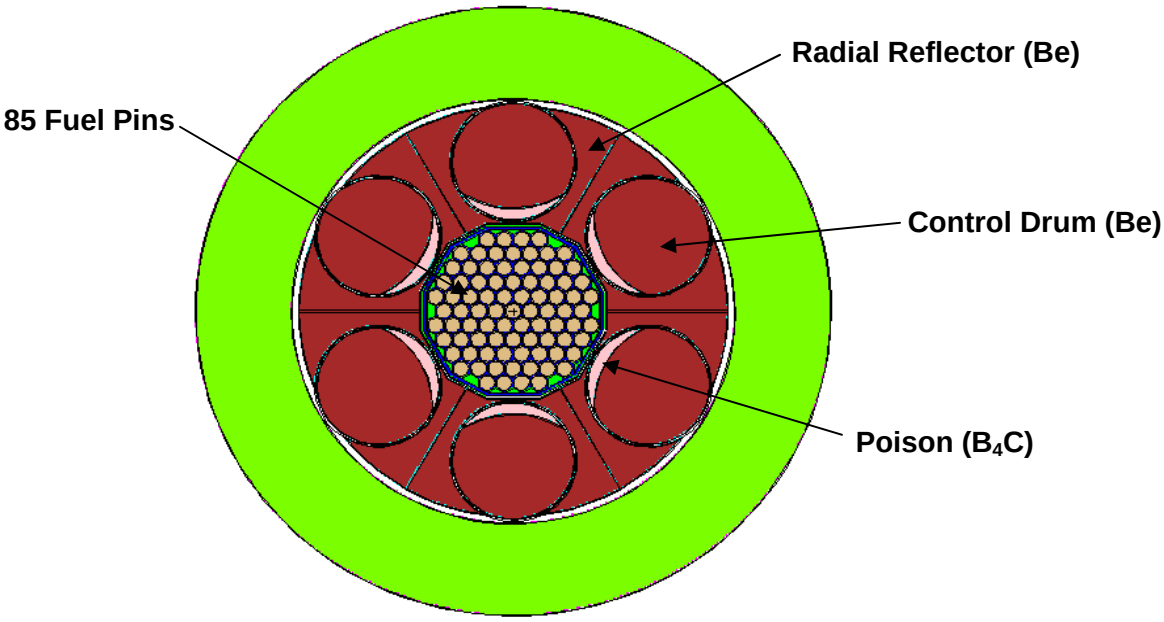

Figure 4-2. Cross Sections of Baseline Design Reactor Core.

Table 4-1. Reactor Design Parameters.

Parameter	Value
Reactor Power (kWt)	101.8
Full-Power Years	5
Number of fuel pins (cm)	85
Fueled core L/D	1.66
Fueled length (cm)	38.0
Fission gas plenum length (cm)	1.0
End cap length (cm)	0.5
Total pin length (cm)	44.0
Pin Pitch (cm)	2.372
Pin OD (cm)	2.108
Fuel pellet OD (cm)	1.994
Fuel clad thickness (cm)	0.051
Nominal BOL/cold fuel/linergap (cm)	0.006
Downcomer thickness (cm)	0.42
Vessel thickness (cm)	0.25
Radial Refl. Be thickness (cm)	15.3
Control Drum OD (cm)	15.7
Max. Drum B_4C thickness (cm)	1.5
Fuel vol., w/2% load void (L)	10.1

5. IMPACT MECHANICAL MODELING

D. L. Villa, J. A. Smith and T. N. Tallman

5.1. Initial Test Cases

The long-term goal of this program was to subject a full-size space reactor design to a high velocity impact event and determine the change in reactivity that resulted. There are many challenges that were faced on the mechanical modeling side as well as the neutronics conversion (DAGMC and DAG-MCNP5) side. To explore these issues and take small steps toward our goal, we used some initial test cases. These cases included a simple cylinder as well as a scaled down full reactor model that only contained 19 pins.

5.1.1. Simple Cylinder

A simple cylinder was used for the initial test of the coupling capability between the impact analysis code and DAG-MCNP5. This single volume was used to demonstrate the work flow before more complicated features were added to the geometry (s*hell elements* or *dead elements*, for example). The details of this analysis will be discussed in the following sections.

The finite element analysis (FEA) work flow consists of developing the geometric model using CUBIT [Sandia 2010], conducting the computation using the explicit Lagrangian finite element (FE) code for modeling transient solid mechanics problems, Pronto3D [Attaway 2000a], and outputting the deformed shape as a function of time in the Exodus [Schoof 1994] format. (Pronto3D was used for the initial development of modeling techniques. The project switched to Presto for the final modeling). To test the workflow and compatibility of the communication between the structural analysis code and the neutron criticality code a simple geometry was created and an impact analysis performed. The structural analysis results were passed to the criticality code to flush out any initial compatibility issues.

The simple geometry for this test problem is a right circular cylinder (height=38 cm, diameter=24 cm) of UO_2-like material that is impacted into a pad of steel with properties of A36 steel [Battelle 1986a] at 40 m/s. Figure 5-1 presents the undeformed meshed geometry and the resulting deformed geometry.

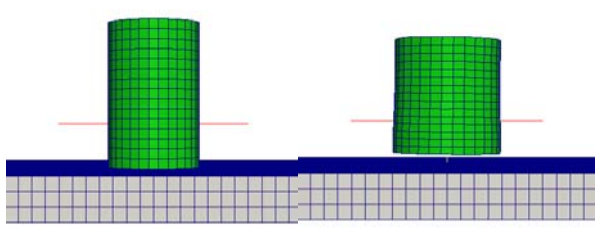

a) undeformed b) deformed

Figure 5-1. Initial Test Geometry.

Currently, the characterization of the mechanical material properties of UO_2 material for impacts at the velocities in the range considered here is not well characterized. An initial literature search did not yield any such properties. Therefore, for the analyses presented here the “Soil-n-Foams”

constitutive model [Attaway 2000a] implemented in Pronto3D was applied using what the authors consider to be UO_2-like properties. The Soil-n-Foams model uses a pressure-dependent yield surface to describe the relationship between the pressure and volumetric strain.

5.1.2. Scaled Down Full Reactor Model (19 pins)

A second test was performed to compare the results of a hand-made MCNP deck with the results from a DAG-MCNP5 deck. A significantly more complicated, 19-pin reactor, geometry was used for the study. The reactor was modeled in both MCNP and SolidWorks. The SolidWorks model was then imported into Cubit for geometry manipulation. Overlapping and duplicate surfaces were resolved and it was then exported as an ACIS geometry file for input into DAG-MCNP5.

The next analysis performed was a 40 m/s impact of the inner core portion of the 19-pin reactor. For the structural impact simulation the structure impacts a pad with the properties of A36 steel. The structural model consisted of the vessel that contains the 19 pins, inner basket which holds the fuel pins, and the fuel pins (containing fuel and reflector pellets). No other materials were modeled. All components were modeled using 8-node hexagonal (hex) elements except for the fuel cladding which was modeled using 4-node shell elements.

The fuel in each fuel rod was modeled as a continuous cylinder of fuel (i.e., individual pellets were not modeled). Again, the UO_2 properties were approximated with the Soil-n-Foams model. The outside diameter (O.D.) of the cylinder of fuel and the reflector pellets matched the O.D. of the fuel pins. The clad shell thickness was specified as the same as that noted in Table 4-1, but the centerline of these shells are located at the O.D. of the fuel rods. The fuel pins were modeled in this way to ensure that the geometry passed to the criticality code was consistent with the geometry of the undeformed structure. The criticality code is not currently capable of taking into account the volume of components modeled with shell elements. Therefore, the fuel and reflector pellets had to include the thickness of the cladding.

The vessel, fuel basket, fuel caps, and cladding were all modeled using an elastic-plastic power law hardening material model with properties compatible with 316 stainless steel [Battelle 1986b]. As with the simple problem discussed above, the impacted pad had A36 steel properties and the fuel used UO_2-like materials. At the time of the analysis the mechanical properties for the reflector pellets were not characterized. To distinguish them from the fuel material they were modeled with the same A36 properties as the impacted pad.

The analysis did not implement any method to include tearing, fracture, or any other form of breaking of material. The 19 fuel pins were free to move and interact with surrounding fuel pins and the basket. The basket and the fuel pins were free to move inside of the vessel. The simulation impact time was 0.100 seconds. This is enough time for the structure to impact and rebound off the impacted pad. The final deformed shape was transferred to the criticality code.

A view of the model before impact is shown in Figure 5-2. The figure shows the portion of the 19-pin reactor modeled with part of the vessel, fuel basket, and some of the fuel pin cladding removed to show the interior of the structure modeled and how the fuel and reflector pellets are

included in the model. The vessel is shown in steel-blue color, the basket shown in yellow, and the fuel rod cladding and caps shown in green, reflector pellets in red, and the fuel in blue. Figure 5-3 is presented to show the relative mesh refinement for the pad, vessel, fuel basket, and fuel pin cladding. For expediency of the calculation the exterior vessel of this model was meshed with a relatively coarse mesh. The fuel basket used a finer mesh. The finest mesh was reserved for the fuel pins (including the reflector pellets and fuel). The mesh refinement of the reflector pellets and fuel was uniform throughout their length. The model has a total of approximately 3.6 million elements and 4.0 million nodes.

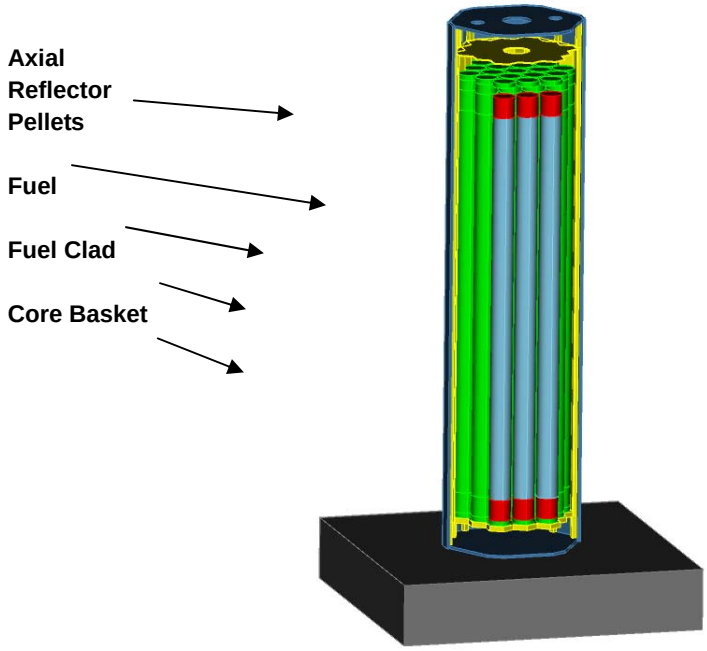

Figure 5-2. Geometry of 19-Pin Reactor FEA Model.

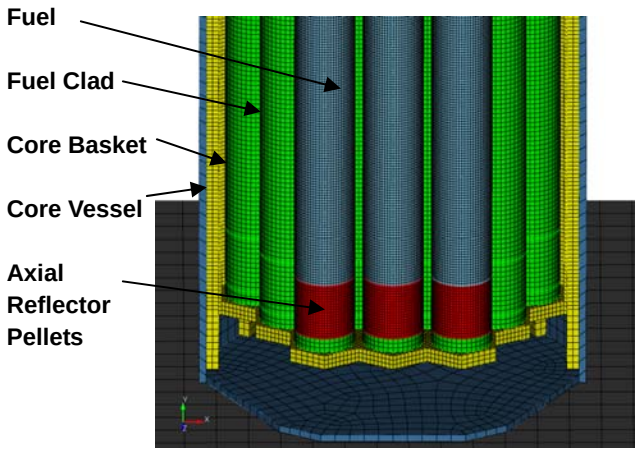

Figure 5-3. Meshed Detail of 19-Pin Reactor FEA Model.

The analysis was performed using the Capacity Computing and Visualization clusters at Sandia National Laboratories. The 19-pin geometry analysis was performed using 300 processors and ran for approximately 24 hours. The overall deformed shape of the geometry (with a portion of

the vessel and fuel basket removed for visualization purposes) is shown in Figure 5-4. The rippled surface on the fuel pins is the steel clad. The fuel pins have become shorter in length and larger in diameter from the impact. Again, this is a preliminary result which may change in detail as the characterization of the mechanical material properties of UO_2 is improved. Figure 5-5 is presented to show the resulting deformed shape of the fuel which has been used as the basis for the MCNP results presented in the next chapter.

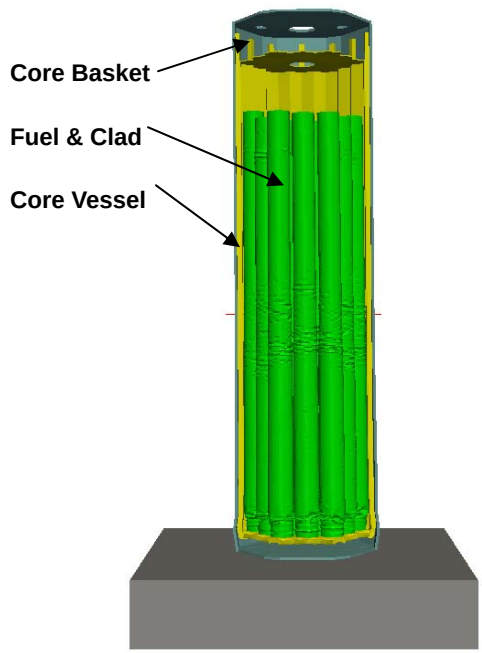

Figure 5-4. Resulting Deformed Geometry of Portion of 19-Pin Reactor Modeled in the FEA.

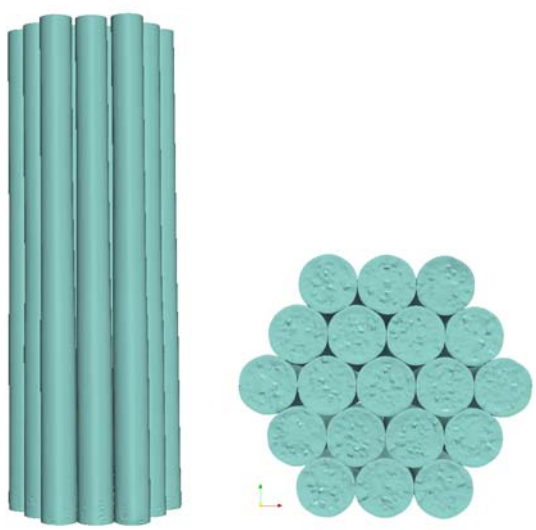

a) Side view b) Bottom view

Figure 5-5. Resulting Deformed Shape of Fuel in the 19-Pin Reactor.

5.2. Geometry and Meshing

The geometry, features, and operation of the eighty-five pin reactor used in this study as a test case are presented by Marcille et al. [Marcille 2006]. The reactor was developed to provide a low cost alternative for space applications. The 101.8kW$_{th}$ design uses a NaK pumped coolant system and UO_2 enriched to 93% ^{235}U clad in stainless steel. Details of the design were not available for model formulation. As a result, some structural performance decisions were made with engineering judgment. A model had been developed in 2009 based on the overall special layout of components. This original model was altered in areas which did not seem to have correct assumptions for structural issues.

The important alterations made were placement of the flow paths for NaK; the nuclear fuel connection to the primary holding plate; the connection method between the inner, outer, and main housing, and making the design gap free. The NaK flow is depicted in Figure 4-1. It starts in the six pipes above the reactor vessel and flows down along the outer boundary of the core in an annular downcomer. It enters a plenum below the core and works upward between the fuel pins as seen in Figure 5-6. Upon entering a chamber above the nuclear fuel, the NaK exits through the central tube at the top of the reactor vessel. The system modeled is cut off at the entrance and exit which leaves the NaK free to flow out as the model deforms.

Figure 5-6 through Figure 5-9 portray the major details of the geometry. Some dimensions are provided but do not fully define the geometry. Unless designated differently, all geometry was modeled as stainless steel 316 (ss316). The system is cut off at the entrance and exit which leaves the NaK free to flow out as the model deforms. A bolted connection at the bottom of each pin was chosen to attach the nuclear fuel to the inner housing (Figure 5-9). Usually, the fuel assembly would have a nut on the other side but this was neglected due to the complexity of the geometry. Spacers at the opposite side from the bolted connection were neglected. The inner and outer housings were connected only at the junction between the NaK entrance on the inner housing and the outer housing. It was assumed that the entire assembly slides together and is then welded through the entire thickness with strengths equivalent to the base material. The geometry was built without gaps since loose parts would lead to failure during random vibration experienced in a rocket launch.

The model was created and archived in solid works if more details are needed. The original model received has also been archived if details of the variations are desired. The reactor was assumed to be symmetric in 30° slices. This allows a “head on” collision which is six times smaller than angular collisions. For angular collisions the geometry was mirrored to produce a half-symmetry model.

Shells cannot be modeled in DAGMC and at least three elements were needed through the thickness to capture bending. The clad thickness was therefore increased from 0.05 cm to 0.1 cm because the explicit time step was limited by the 0.017 cm length required. 0.1 cm was considered acceptable due to the undeveloped nature of the design. Several other locations with thinner shells were also increased to 0.1 cm.

The mesh was created in Sandia's mesh generation tool Cubit [Sandia 2010]. The NaK fluid geometry was developed in Cubit by subtracting all of the solid volumes. It was assumed that the entire chamber contained NaK. The UO_2 and B_4C were cut up into small pieces in cubit to approximate expected cracking. The number of divisions was larger for the 1/12th head on model than the ½ angular collision models because the number of volumes was too large for use at UWISC. Cubit becomes much slower as the number of volumes rises to several thousand.

Modeling the coolant posed a problem initially because of the large "distortion" expected as the fluid moves under impact. The problem was solved by using SPH elements [Swegle 1994], which has been used in the past to model impacts in water. Presto handles overlaps with SPH elements by moving solid elements until no overlap exists. It was found that the SPH elements created overlaps which cut through the entire length of elements in the nuclear fuel clads as seen in Figure 5-10. No remedy to this situation could be found through use of input parameters. As a result, a Fortran program was developed to reduce the SPH radius sizes to zero overlap. This program is explained in Appendix A of the report on reactor impact modeling [Villa 2010].

The 1/12th symmetry mesh has 1,439,347 nodes and 1,049,021 elements. Of these elements 80,881 are SPH elements for the water shield and NaK working fluid. The full half-symmetry model has 8,222,433 nodes and 6,385,558 elements. Of these elements 324,006 are Nak SPH elements and 161,280 are water SPH elements.

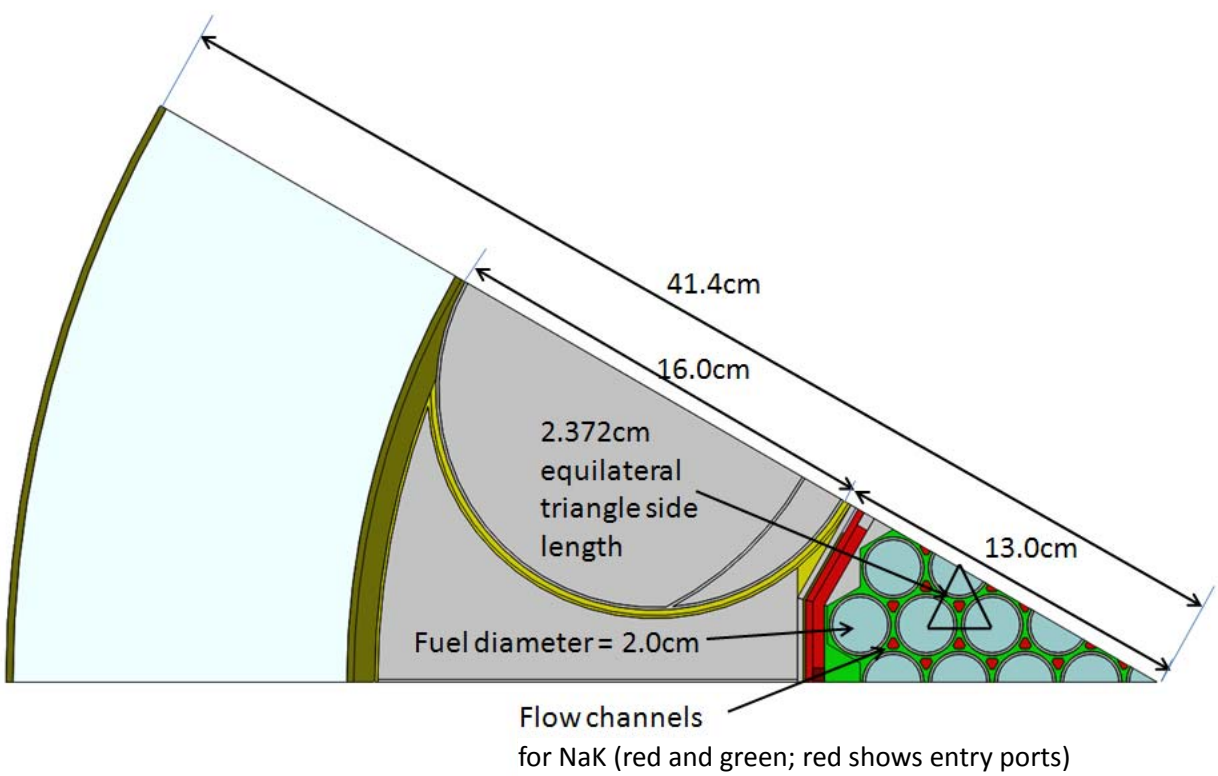

Figure 5-6 Horizontal Cross Section of Geometry from Top.

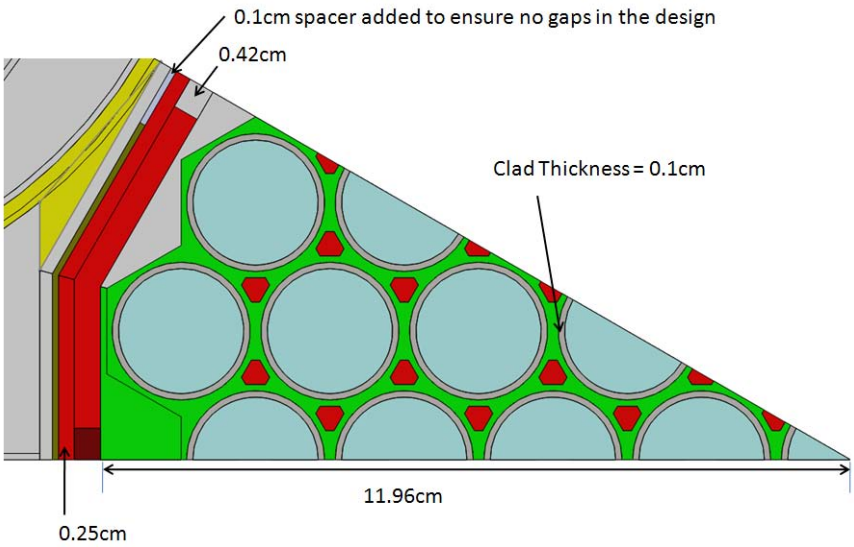

Figure 5-7 Detailed View of Nuclear Fuel Cross Section.

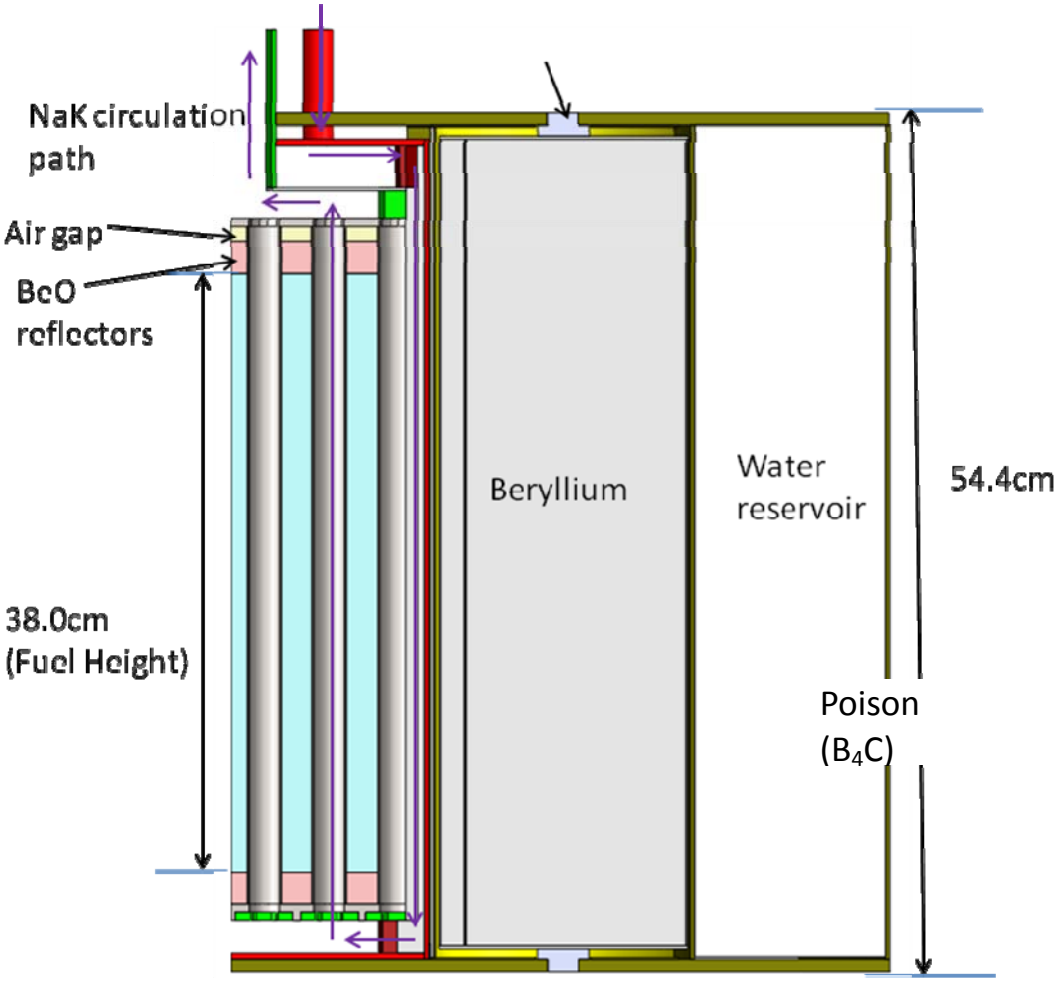

Figure 5-8. Vertical Cross Section of Geometry.

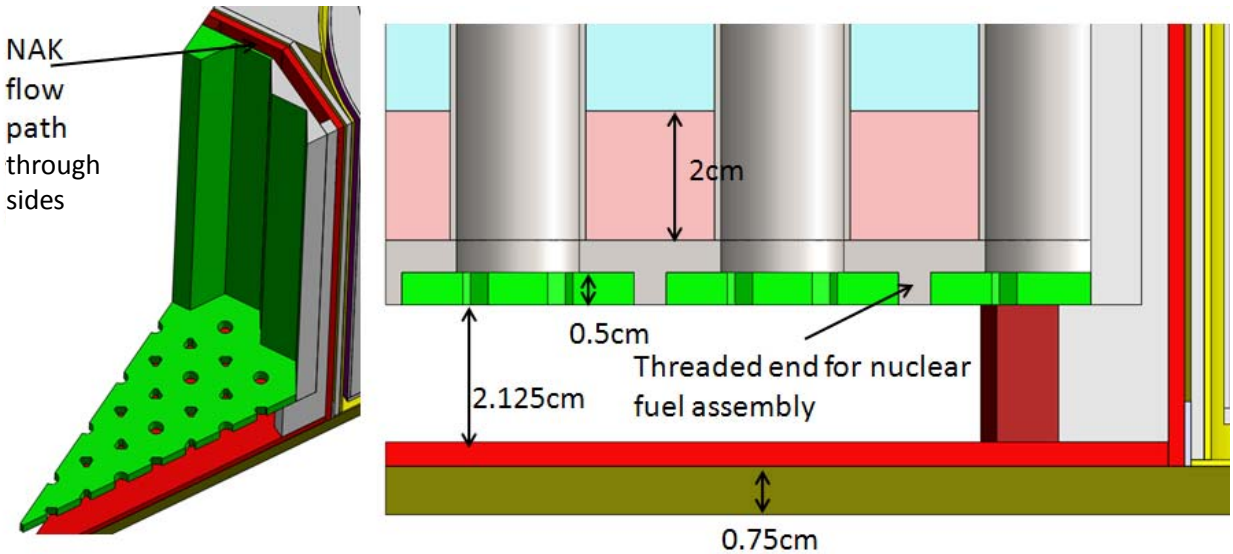

Figure 5-9 NAK Flow Illustration and Other Details.

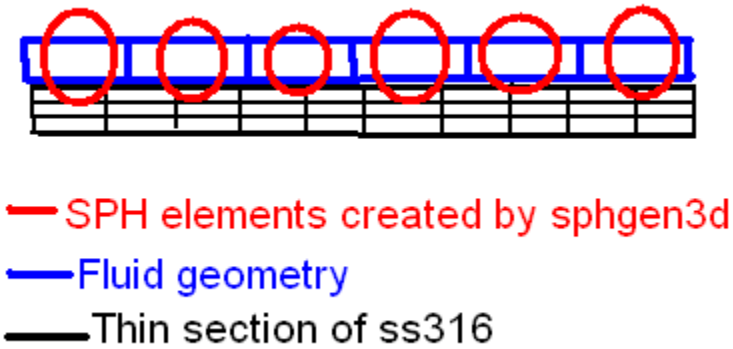

Figure 5-10. SPH Overlap Illustration.

5.3. Material Properties

Literature and web searches were done to obtain realistic material properties. Considerable investigation into the range of uncertainty for material properties was unnecessary since the analysis was a demonstration. Rate effects were neglected and all properties were for quasi-static conditions at room temperature. The properties have both typical values and specific values which were obtained from an individual set of testing. All of the material properties are recorded in the tables which follow. The references given are separated by commas and correspond to the material properties from left to right. References surrounded by parenthesis designates that a given material property comes from a compilation of more than one source.

Death criteria are portrayed in Table 5-2 and were chosen based on the maximum principal logarithmic strain. The equivalent plastic strain (eqps) criteria for Be and SS316 are large values beyond the expected tensile failure which do not have any physical basis other than to assure that the problem solution does not become overly deformed. All of the materials included death by inversion.

The concrete constitutive behavior was chosen to be represented by the K&C concrete model which is presented in detail by Malvar et al. [Malvar 1997] and is summarized by Brannon and Leelavanichkul [Brannon 2009]. All of the input required is contained in Table 5-1, Table 5-4, Table 5-5 and Table 5-6. All of the inputs are based on a concrete calibration effort presented by Attaway et al. in [Attaway 2000b]. Refer to appendix C of [Attaway 2000b] for more details. The compressive strength of 4000psi is an extrapolation of the data contained in [Attaway 2000b]. Since the analysis of the reactor is a demonstration, the concrete model was used as provided.

The water shield and NaK used an elastic model with the bulk modulus of water (2.2GPa) and Poisson's ratio of 0.49. Even though this is not a fluid constitutive model, this provides a correct pressure response with negligible deviatoric resistance.

Table 5-1. Material Constants Used.

Material	Material Name in Input File	Elastic Modulus g/cm-s^2	Pois-son's Ratio	Density g/cm^3	Yield Stress g/cm-s^2	Reference
Uranium Dioxide	UO2	1.803E+12	0.286	9.873	N/A	Phani 1986,Kutty 1987,Wikipedia 2010
Boron Carbide	B_4C	4.640E+12	0.180	2.52	N/A	Kutty 1987,Bourne 2002,Bourne 2002
Beryllium Oxide	BeO	3.450E+12	0.380	2.85	N/A	Matweb 2010,Azom 2010,Matweb 2010
Stainless Steel 316	Ss316	1.938E+12	0.294	7.91	1.670E+9	(Lee 1998,Ledbetter 1981),SSINA 1998,Michel 1973
Beryllium	Be	3.030E+12	0.075	1.85	2.067E+9	Marder 1986,Matweb 2010,Marder 1986,Goods 1998
Concrete	concrete_ target	2.486E+11	0.190	2.27	2.756E+8*	Attaway 2000b

*Compressive strength

Table 5-2. Death Criteria Used.

Material	Criteria Variable	Threshold	Criteria Variable	Threshold	Reference
Boron Carbide	Max principal stress	>3.00E+9	Min principal stress	<-2.85E+10	Shackelford 2001
Stainless Steel 316	Maximum principal logarithmic strain*	>=0.432	eqps	>=1.2	Michel 1981, stability guess
Beryllium	Maximum principal logarithmic strain*	>=0.04653	eqps	>=0.25	Goods 1998, stability guess

*For earlier runs tensile_eqps criteria were used but this variable was not applicable to hexahedral elements.

Table 5-3 Multilinear Stress Strain Curves for SS316 and Be.

stainless steel 316 (from [Goods 1998**])**		**Beryllium (from [Marder 1986])**	
eqps	stress g-cm/s^2	eqps	stress g-cm/s^2
0.0	0.0	0.00E+00	2.07E+09
5.92E-03	5.03E+08	6.24E-04	2.34E+09
9.47E-03	8.03E+08	1.65E-03	2.42E+09
2.00E-02	1.23E+09	4.33E-03	2.73E+09
3.90E-02	1.64E+09	8.03E-03	3.08E+09
6.20E-02	2.06E+09	1.08E-02	3.29E+09
8.20E-02	2.43E+09	1.47E-02	3.47E+09
1.14E-01	3.05E+09	1.96E-02	3.64E+09
1.63E-01	3.92E+09	2.54E-02	3.76E+09
1.87E-01	4.26E+09	3.12E-02	3.84E+09
2.17E-01	4.65E+09	3.60E-02	3.89E+09
2.56E-01	5.13E+09	4.18E-02	3.93E+09
2.93E-01	5.55E+09	4.65E-02	3.95E+09
3.29E-01	5.92E+09	2.00E+01	1.00E+11
3.73E-01	6.36E+09	-	-
4.05E-01	6.65E+09	-	-
4.32E-01	6.85E+09	-	-
1.00E+02	5.14E+11		

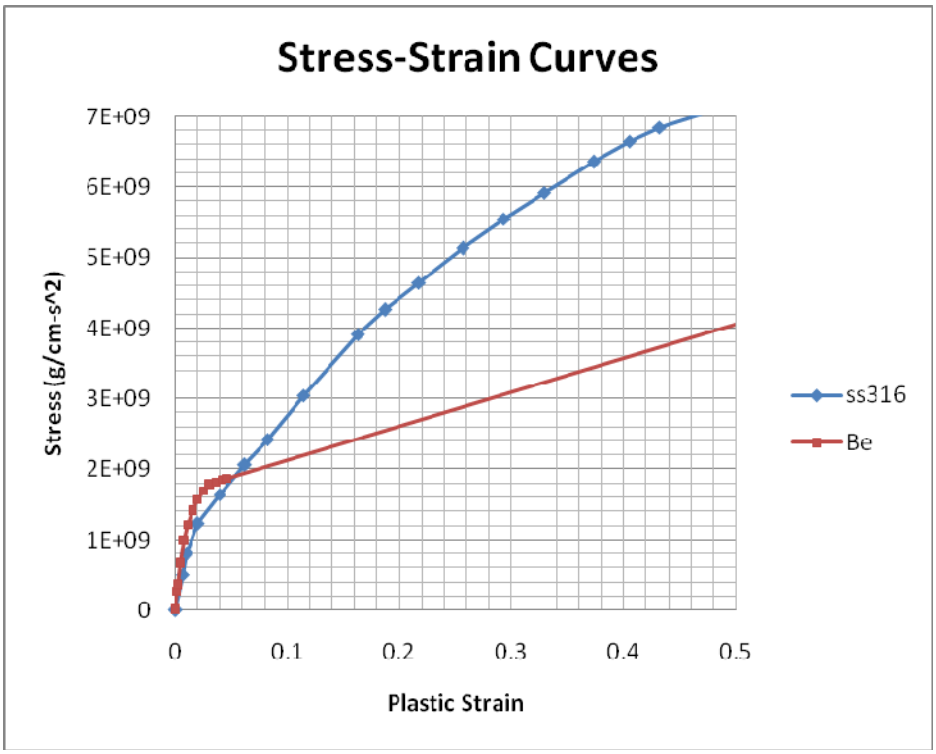

Figure 5-11. Stress-Strain Curves for Beryllium and SS316.

Table 5-4. Additional Concrete Parameters.

Concrete Parameter Name	Unit	Value
Tensile Strength	g/cm-s^2	2.922E+7
Fractional Dilatancy	-	0.5
Lambdam	plastic strain	5.6E-5
Lambdaz	plastic strain	5.70E-4
Maximum Aggregate Size	cm	0.9525
One Inch	cm/in	2.54

Table 5-5. Damage Function and Dynamic Increase Factor Function for Concrete.

Effective plastic Strain Parameter (λ)	Damage Function (η)	Strain Rate 1/s	Dynamic Increase Factor
0.000E+00	0.000E+00	-3.000E+06	1.218E+01
8.000E-06	8.500E-01	-3.000E+02	1.218E+01
2.400E-05	9.700E-01	-1.000E+02	8.448E+00
4.000E-05	9.900E-01	-1.000E+01	3.921E+00
5.600E-05	1.000E+00	-1.000E+00	1.820E+00
7.200E-05	9.900E-01	-1.000E-01	1.647E+00
8.800E-05	9.700E-01	-1.000E-02	1.491E+00
3.200E-04	5.000E-01	0.000E+00	1.000E+00
5.200E-04	1.000E-01	1.000E-02	1.221E+00
5.700E-04	0.000E+00	1.000E-01	1.322E+00
		1.000E+00	1.431E+00
		3.000E+01	1.608E+00
		1.000E+02	2.402E+00
		3.000E+02	3.465E+00
		3.000E+06	3.465E+00

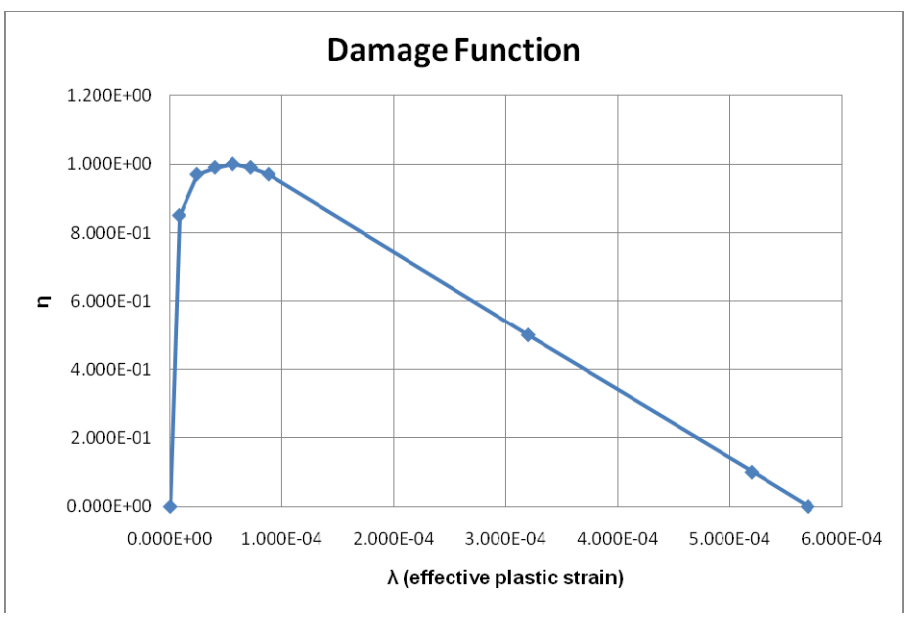

Figure 5-12 Concrete tensile damage function.

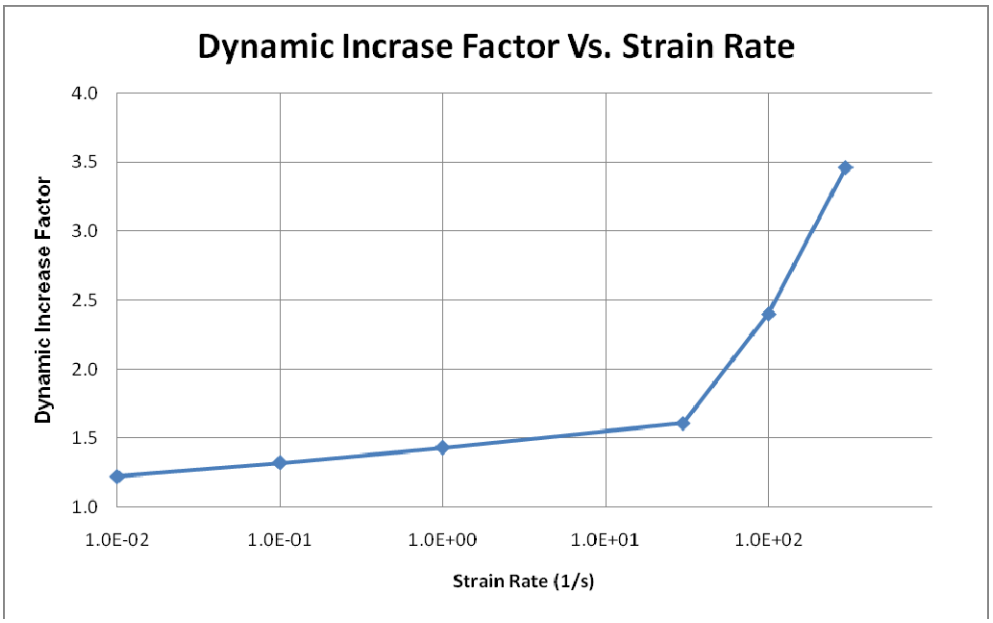

Figure 5-13. Dynamic Increase Factor vs. Strain Rate.

Table 5-6. Concrete Pressure and Bulk Modulus Functions.

Volumetric Strain	Pressure g/cm-s^2	Bulk Modulus Load Unload g/cm-s^2
0.00E+00	0.00E+00	1.34E+11
1.50E-03	2.00E+08	1.34E+11
2.70E-03	3.07E+08	1.35E+11
4.30E-03	4.37E+08	1.37E+11
6.00E-03	5.49E+08	1.40E+11
8.00E-03	6.27E+08	1.42E+11
1.97E-02	1.03E+09	1.58E+11
8.90E-02	4.35E+09	2.51E+11
1.00E+00	4.45E+10	1.34E+12
1.00E+03	4.47E+10	1.47E+12

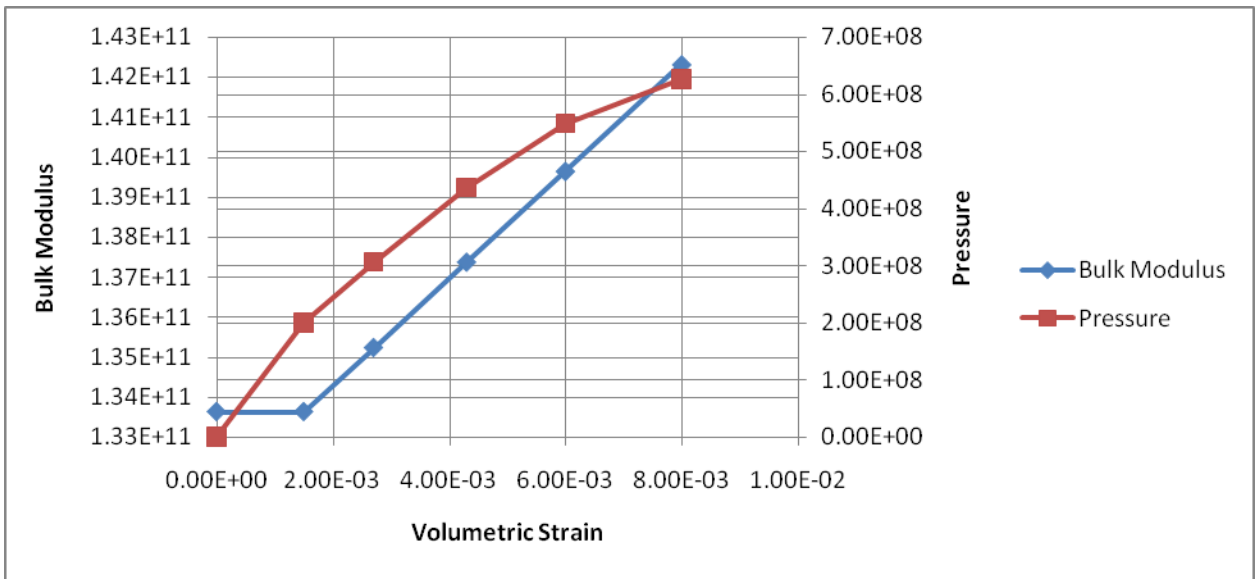

Figure 5-14. Concrete pressure and bulk modulus vs. volumetric strain functions.

Table 5-7. Fluid Properties.

NaK, water		**Air**	
K (g/cm-s^2)	2.2e10	Rho_0 (g/cm^3)	0.001225
ν	0.49	C_0 (cm/s)	3430
		Gamma (heat capacity ratio)	1.4

Table 5-8. UO_2 Soil and Foam Properties.

UO2 Soil and Foams Parameters	**Reference/Note**	
A0	1.500E+8	[Evans 1969]
A1	0.0	No data to fit
A2	0.0	No data to fit
Pressure cutoff	-1.500E+8	[Evans 1969]
Pressure Function (volumetric strain vs. pressure g/cm-s^2)	0.0 0.0 0.1 2.15526E+10 1.0 2.15E+12 100.0 2.15E+14	1/10 of the bulk modulus until 10% porosity is fully compacted followed by the full bulk modulus of UO2

The ceramic materials were difficult to model because of the brittle fracture which occurs for impacts. Element death is usually not an appropriate method to deal with these problems because the algorithm removes an excessive amount of the mass as the ceramic impacts other parts. Alteration of the connectivity of the mesh by disconnecting the elements or by replacing the element with an SPH particle makes the problem less stable and changes the mesh topology. For lack of a better alternative, the nuclear fuel was split into multiple pieces with the assumption that pre-existing flaws made fracture across the entire length occur regardless of impact energy. For the 1/12th symmetry model the cut patterns consist of one centimeter sections of the cylindrical pins which have been sliced at ninety degree angles as seen in Figure 5-15.

The only exception to this pattern is the central pin which is cut at thirty degree angles. The orientations of the ninety degree cuts normal to the length of the fuel pins were not controlled in any special way and were placed at either zero or thirty degrees as seen in Figure 5-15. Several volumes have been hidden in Figure 5-15 in order to enable visualization of the shape of the pin cuts.

The nuclear fuel was assumed to have ten percent porosity. All of the other properties were scaled to reflect a porous material. No available data concerning compaction of UO_2 was found. It was therefore assumed that a linear compaction occurred at one-tenth of the fully compacted bulk modulus followed by return to the bulk modulus once zero porosity had been reached. The soil and foams model in Presto was used to include a compaction equation of state. For this model, the deviatoric response of the model is elastic perfectly plastic with a yield stress of 150MPa. All of the UO_2 data is provided in Table 5-8.

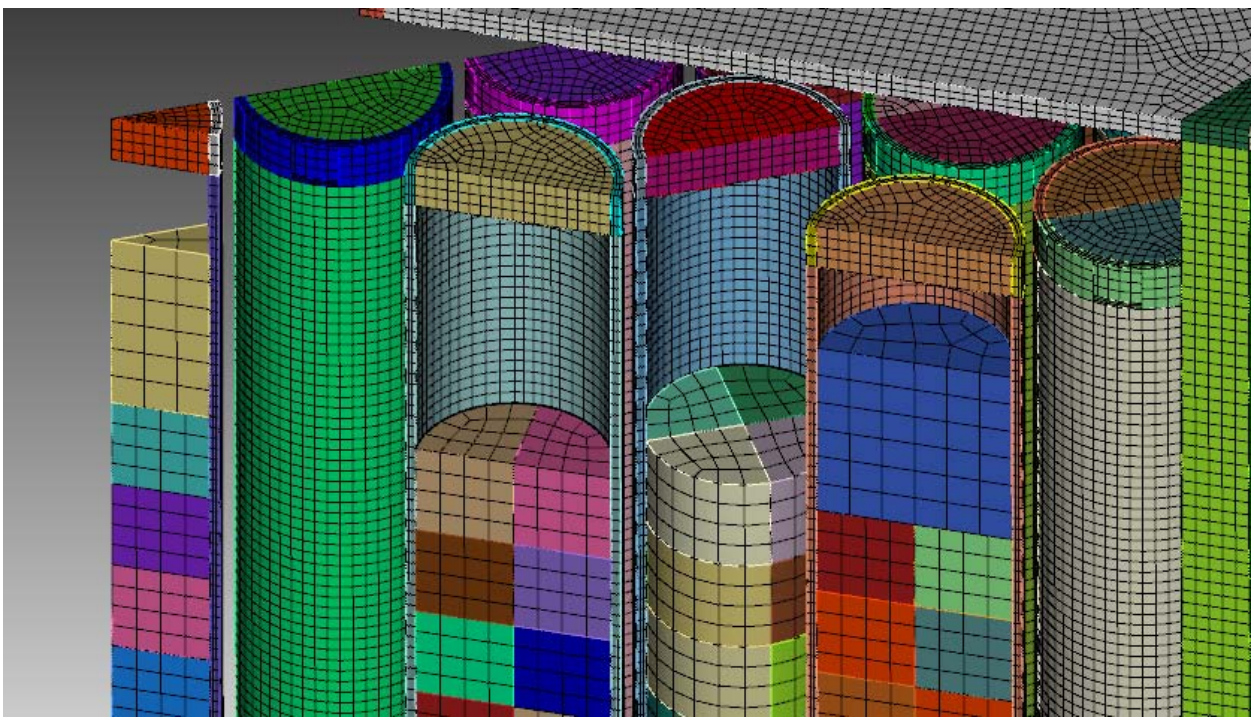

Figure 5-15 1/12th symmetry model Cuts in UO_2 Fuel.

5.4. Computational Details

All of the analyses were accomplished using Sandia National Laboratory's code Presto version 4.16.2. Any references to specific models or features in Presto can be found in the version 4.16.2 manual [23]. The following statement from Presto's internal website summarizes its capabilities:

PRESTO is a three-dimensional explicit, transient dynamics code with a versatile element library, nonlinear material models, large deformation capabilities, and scalable contact. It is built upon the SIERRA Framework, which provides a data management framework in a parallel computing environment that allows addition of capabilities in a modular fashion.

Eight-node, under-integrated, hexahedral elements and smoothed particle hydrodynamic (SPH) elements [Swegle 1994] were used in the simulation. The hexahedral elements were used with all of the defaults for hourglass parameters, bulk viscosity, and strain incrementation of Presto 4.16.2. Three elements were maintained through the thickness of all thin sections. Some of the thinnest stainless steel sections were excluded in an effort to minimize the element count. They had originally been meshed but were eliminated because they contained a large fraction of the total elements but provided insignificant structural support during the collision event. Their thin cross sections also make them negligible to the DAGMC analysis. Analyses were executed at 100 m/s against concrete at impact angles of 0°, 10°, 45°, and 90°. The angle convention is shown in Figure 5-16.

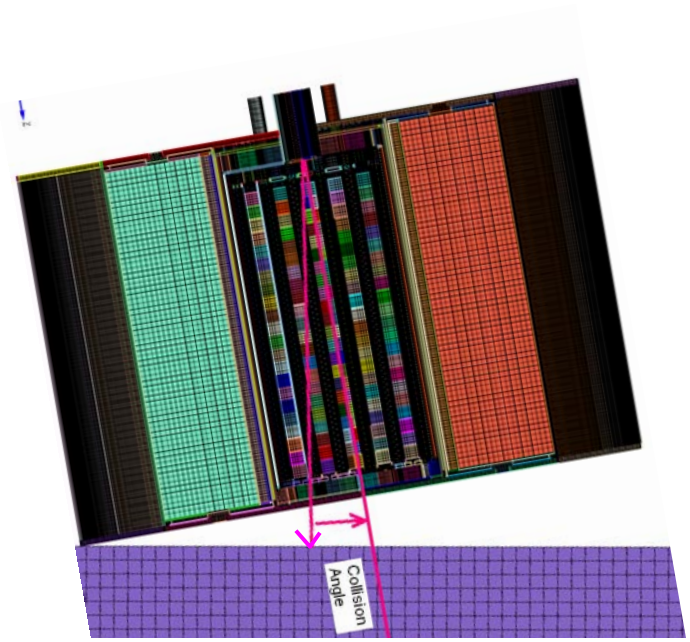

Figure 5-16. ½ Symmetry Model, Collision Angle Convention and View of Cuts in the Fuel Pins.

Passing data to UWISC requires a specific procedure to assure that the data can be interpreted by DAGMC. In the future much of the manual part will be eliminated. The process is summarized in Figure 5-17 and explained in detail in the list of steps below. References to “the solid portion of the mesh” point towards all of the elements which are hexahedra. References to the “fluid portion of the mesh” refer to two separate regions in the model which are the NaK working fluid and water shield surrounding the reactor. Each of these regions must be isolated and processed separately in the steps to building the model.

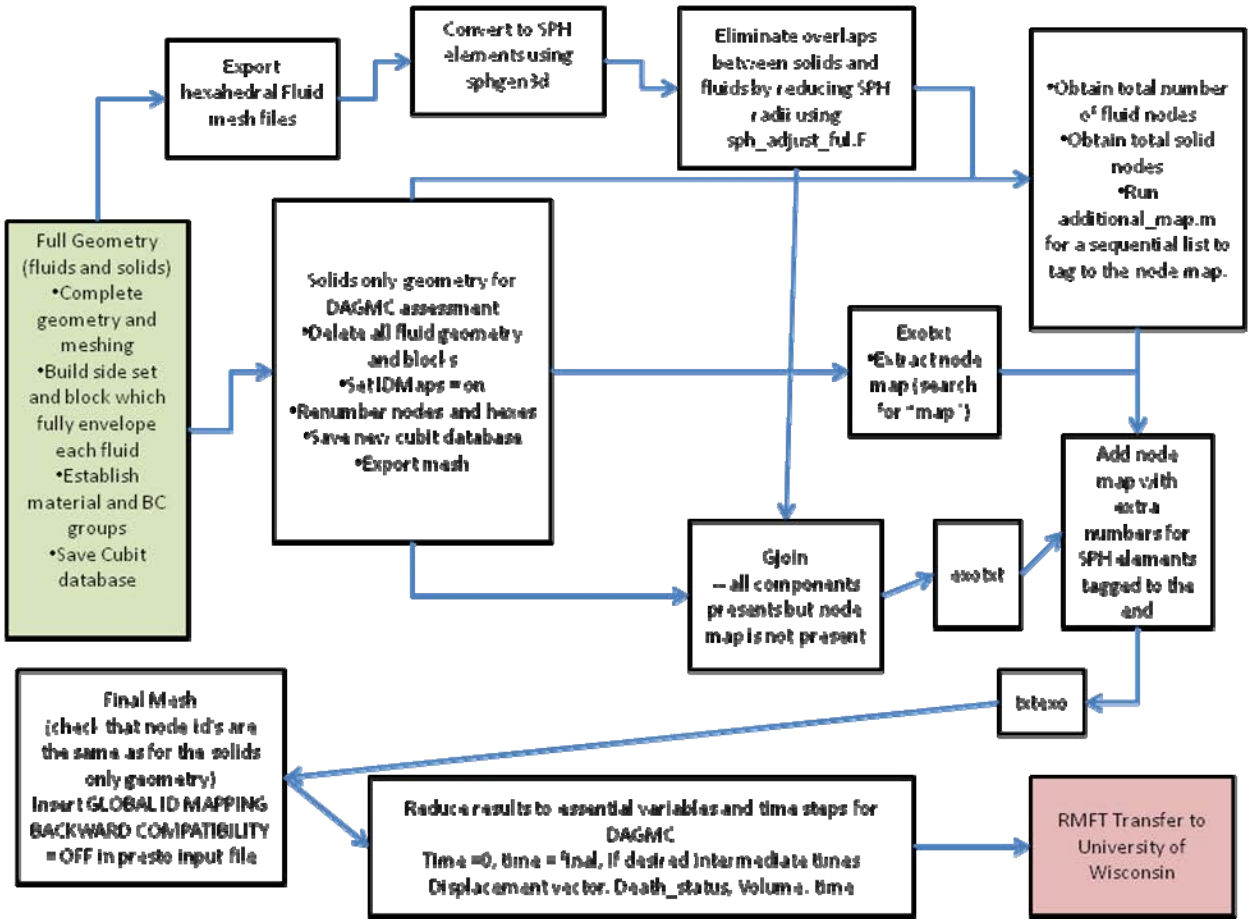

Figure 5-17. Procedure to Communicate with DAGMC.

This process requires use of the Sandia engineering analysis code access systems (SEACAS) [Sjaardema 1998] mesh manipulation tools grepos, gjoin, sphgen3d, grope and algebra. These tools are available through contacting the author of [Sjaardema 1998].

Refer to Figure 5-17 for an overview of the process required to communicate from Presto to DAGMC. Geometry creation and meshing need to be completed before proceeding. The geometry must be in centimeters for use in DAGMC. Care should be taken to check that the model has the desired intent. This cannot be overemphasized because producing a mesh usually involves a single export command in Cubit. Building a mesh with SPH and solid elements for use in DAGMC takes several hours. This is driven primarily because of the need to preserve node identification numbers in cubit (e.g. node 1 in cubit is equal to node 1 in the results database).

It was discovered that the process of passing information from Presto to DAGMC was very sensitive to details. Hence a very specific process was developed, documented and adhered to. The process is listed below:

1. All of the materials should be defined as blocks. Groups should be created with names which indicate the material and density for each block. Side sets and node sets should

also have groups which have a name indicating their use in the analysis. For example, for block 17 a group should be created named UO2_9_87 indicating the material is uranium dioxide of density 9.87g/cm^3. A node set could be placed in a group called "fixed," and a side set could be called "symmetry." Dummy shell blocks and side sets which consist of all of the surfaces on the solid mesh which surround the fluids need to be created with one block per fluid region. These blocks will not be used in the analysis but are required in the Fortran script which eliminates SPH overlap (Appendix A of Villa 2010). Issue the command "set geometry version 1600" and save the database so that it can be opened using cubit 10.2 which is the version currently used at UWISC. Assign a name which indicates that all geometry including the SPH geometry is present.

2. Export the mesh with all blocks. Use grepos to isolate the blocks which are fluids and the corresponding dummy blocks and sidesets. Also use grepos to create files which contain the corresponding dummy shell blocks which consist of the solid interfaces to the fluid.

3. Convert the hexahedral fluid meshes to SPH elements using sphgen3d. This produces SPH meshes which will have overlaps with the boundaries of the solid portion of the mesh (Figure 5-10).

4. Join the dummy shell block mesh files and the SPH fluid meshes into a single file using gjoin for each fluid region.

5. Use the Fortran program "sph_adjust_full.f" to eliminate overlap. Care must be taken because several manual inputs are needed as described in Appendix A of Villa 2010. Sufficient detail is given to compile and run the program on a unix platform which has access to the exodus database libraries.

6. Use grepos to strip off the dummy shell blocks and sidesets so that only the adjusted SPH elements remain.

7. Returning to the cubit database, save with a new name which indicates that it is the database which will be passed to UWISC. Proceed to delete all of the fluid blocks and geometry. Also delete the dummy shell blocks and sidesets which were created to envelope the fluid geometry. Issue the command Set IDMaps=on and renumber the nodes and hexahedral elements using "renumber node all uniqueids" and "renumber hex all uniqueids." Issue the command "set geometry version 1600" and save the database.

8. Convert the mesh file which was just exported into a text file using exotxt. Open the text file and search for "map." This should bring the cursor to the beginning of the node map which has to be manually inserted into the joined results. Currently none of the SEACAS utilities retain node maps and a manual work around is inevitable. Record the line number and search for map again. This will bring the text to the end of the node map. Cut and paste the node map into a new text file. One way to make this easy is to use vi. Press ":" and enter the text "r! sed –n n1,n2p file" where n1 and n2 are the line numbers of the beginning and end of the node map and file is the path and file name of the exotxt output (e.g. r! sed –n 4264365,5865467p ./solids.txt).

9. Open up the SPH element genesis files using grope and record the total number of SPH nodes for all fluid regions. Open up the solid region mesh and record the number of nodes in it. Open the matlab script additional_map.m (Appendix B of Villa 2010) and enter the parameters at the beginning of the script. This script creates a list of numbers counting up by increments of one from the last solid node number up to the final SPH element. "begin_node" is the number of solid region nodes plus one. "end_node" is the number of solid region nodes plus the number of SPH nodes. Open the solid region node map and move to the end. See how many lines are filled with a node number on the final line (will be a number between 0 and 8). Enter this number for the "skip_places" parameter. This will cause the text to write out so that the two node maps can be aligned. Run additional_map.m in matlab. This map will be tagged to the original node map to form a complete node map which will work when the fluid and solid regions are joined.

10. Use gjoin to join the solid and fluids regions. The solid region must be first.

11. Convert the combined mesh into a text file using exotxt and replace the line "sequence 1...numnp" with a line with the words "explicit map" insert the complete node map constructed in step 9 into the text file and eliminate all blank lines. Save and exit the text file and use "txtexo" to convert it back into a genesis file. If the process fails to convert then check that the node map you are inserting has the exact same number of nodes. The syntax must be exact or else txtexo will fail.

12. Verify that the node numbers in the resulting file line up with the cubit database saved in step 7. Do this by checking the coordinates of a couple of random nodes and see if they correspond to the same coordinates in Cubit. Grope is a good tool for doing this.

13. In the Presto input file insert the following line in the finite element definition section ("begin finite element model *model_name*")

    GLOBAL ID MAPPING BACKWARD COMPATIBILITY = OFF

    Even though OFF intuitively seems like the incorrect setting it is correct.

14. Insert the following essential variables in the output which are needed by DAGMC. Other variables can be added but will need to be stripped out of the database after the run.

    nodal variables = displacement
    element variables = volume
    element variables = death_status
    global variables = timestep

    The time is also needed but this is a natural portion of the database which marks each other variable.

15. Run the analysis. If any error is found which requires updating the cubit databases and repeat all steps 1-14. Verify that the output databases have the same numbering scheme as the cubit file from step 7 once an output file has been produced. If the node numbering scheme is not identical, the results cannot be processed by DAGMC.

16. Post process the output using "algebra." Eliminate most of the time steps. Ten time steps is a good number to retain in order to capture criticality trends with time. Delete all variables except those listed in step 14.

    If results are going to be calculated externally, send the cubit database and exodus results file to the pertinent contact using Sandia's remote file transfer (RMFT) tool located at the following website: https://mft-srn.sandia.gov/

5.5. Impact Results

The objective of the analyses presented was to provide realistic reactor deformed geometries to DAGMC so that geometry transfer and modeling techniques could be developed, and to demonstrate robust reactivity assessments. The results therefore do not have any requirements for post processing and interpretation. Even so, it is hoped that comparisons between the model with and without SPH elements will serve to show that including fluids within the system is important. It can be argued that the change in analysis energy balance makes including the fluid necessary. The working fluid and water shield in the eighty-five pin reactor increase the mass by 28.5%.

It would be extremely difficult to model the inertial and contact interactions in any other way than a fully coupled approach because the fluid load transmission is complex. Alternatives to the SPH approach should be investigated. For example, using a two-way interaction which feeds geometry to the fluid analysis and a pressure distribution to the structural analysis may prove to be a more robust method. The computational expense of such an effort may outweigh the benefits though.

The zero degree collision was accomplished with and without SPH elements. A visual inspection of the results in Figure 18 reveals some key differences. The presence of the water causes the water shield containment to tear at the top. The opposite effect occurs at the NAK exit. Due to the presence of NAK, the exit does not tear in two but remains intact. The additional mass of the water compresses the concrete target with a wider footprint and lessens the slope between the reactor and target at the fuel. The most important effect observed is that the fuel experienced 32% greater engineering strain for the center fuel pin without SPH elements as seen in Figure 19. The presence of the SPH elements serves as a cushion whose properties are dictated by the NAK viscosity and bulk modulus. As the NAK is compressed, it begins to flow out of the chamber below the fuel. It goes up the passageway which was designed to allow flow for heat exchange. The high velocity impact leads there to be a sudden onrush which deforms the stainless steel surroundings. A jet of NAK forms as seen in Figure 20. At the beginning of the simulation the NAK transmits load more quickly and has a stiffer response than the no SPH run.

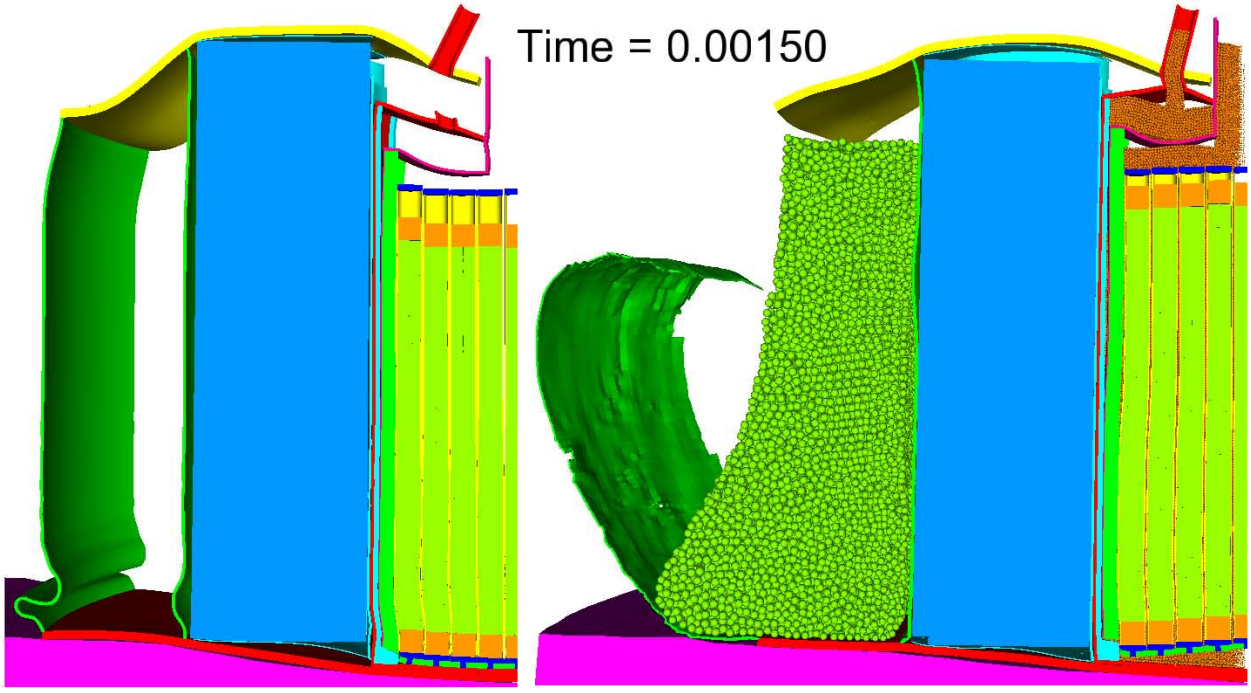

Figure 18 Zero Degree Collision with and without SPH Elements.

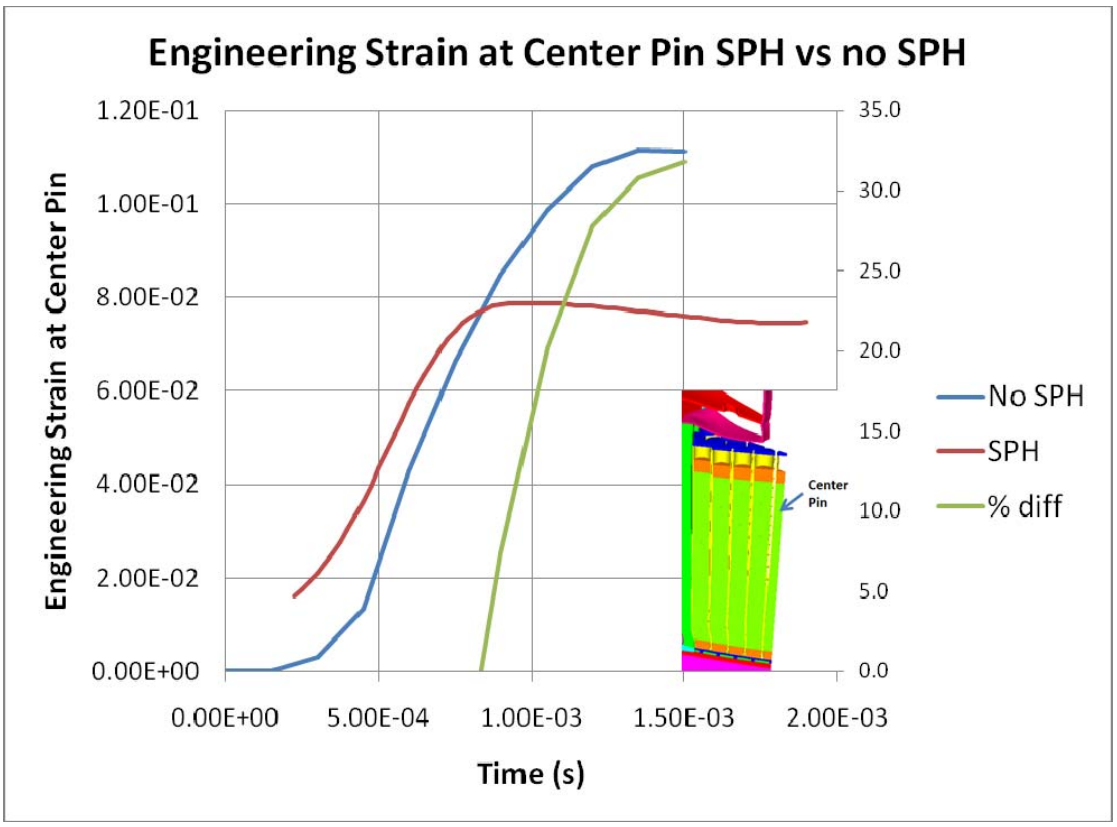

Figure 19 Strain at Center Pin.

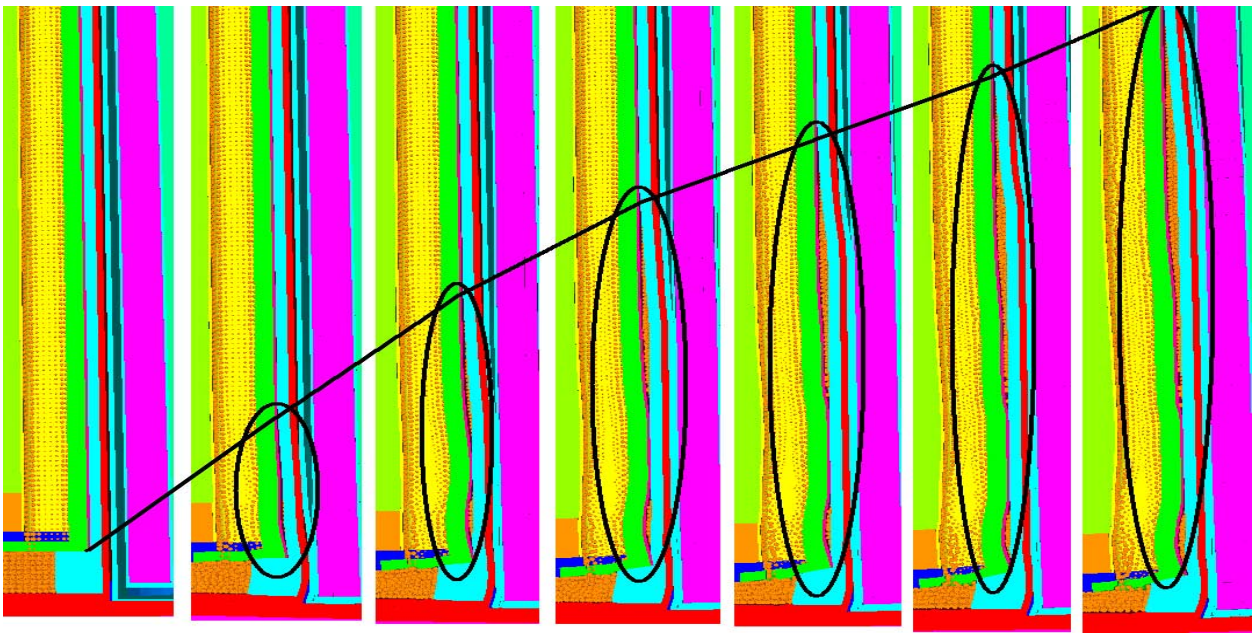

Figure 20. Advancing NAK Jet.

As time progresses, the NAK SPH elements act as a shock absorber and dampen out the KE through the upward jet of NAK flow. The non SPH model suddenly comes into contact with stainless steel with little of the KE of the fuel dissipated. The fuel subsequently crushes and expands in the radial direction much more than the SPH case.

The model is not currently calibrated sufficiently to expect that the model captures NaK energy dissipation. No viscous properties are available in the elastic model used and the fuel behavior at high strains is not well understood. The behavior does highlight the importance of including the working fluid though. Even though dynamic effects are not accurately captured by the current elastic fluid model, this illustrates that the fluid structure interaction contains all of the required large deformation kinematics and that the behavior is intuitively correct.

The differences in reactivity due to these modeling differences are discussed in the next chapter. Even though the zero degree case clearly demonstrates the need for including the working fluid, the forty five degree case deformation can be argued to be less sensitive based on the deformation shown in Figure 21. If an SPH run had been completed it would be expected that the water shield would once again burst but the plate below the nuclear fuel has sufficient strength at this angle to support the fuel and the primary factor in deformation of the fuel is the beryllium shield. The reactivity results for the 45 degree simulation without SPH elements are also in the next chapter.

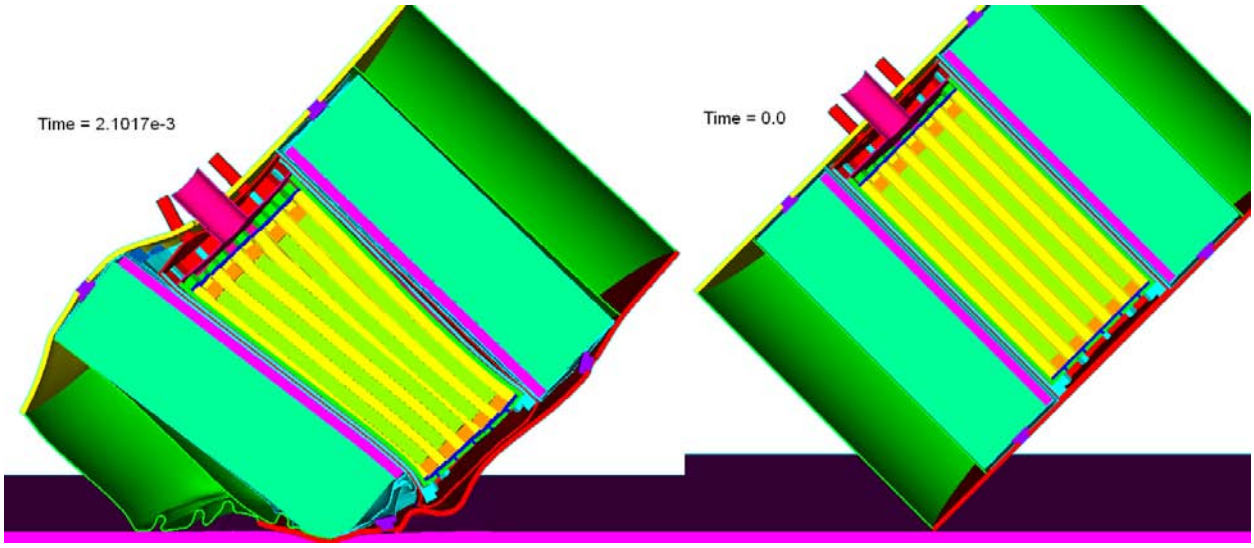

Figure 21 Final Time Calculated for 45 Degree No-SPH Simulation.

One difficulty encountered in SPH to hexahedral interactions is that SPH elements tend to excite hourglass modes under high pressure. This is especially true for incompressible fluids (Poisson's ratio = 0.5) but also occurred for Poisson's ratio of 0.49. This behavior is illustrated in Figure 22. Eliminating this behavior would be difficult because the underlying problem is the presence of hourglass modes. Some sort of smoothing between the SPH elements and hex elements would probably solve the problem but would increase computational expenses drastically. A better alternative may be to alter the methods used to increase and decrease the contact radius of the SPH elements in order to keep the pressure uniform under dynamic conditions. This would occur by slightly shrinking areas of high pressure and expanding areas of low pressure. Such ideas need further exploration to prove whether the concept will solve the problem with a single local function input.

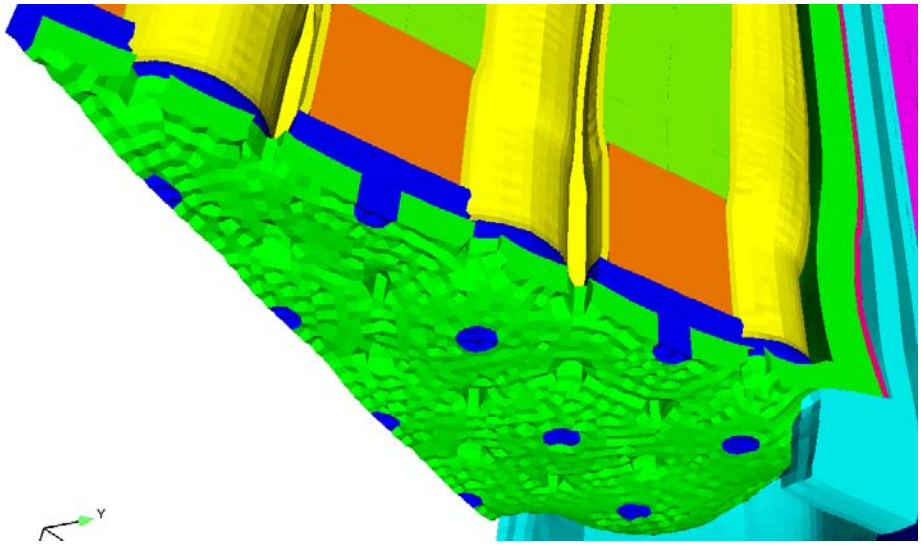

Figure 22. Hourglass Aggravated Surface Due to High Pressure SPH Contact Interactions.

5.6. Future capabilities

There are many capabilities which would considerably enhance the current ability to couple deformed geometry and reactivity assessments.

1. The ability to use shell and SPH elements in Presto would considerably decrease the computational expense of doing reactivity assessments. This would require that DAGMC be able to handle lofted geometry. Development of a robust 8 node hexahedral shell (hexshell) element which can interface with solid 8 node hexahedra would also meet this need.
2. Eliminating the need to maintain node number id's in DAGMC would simplify the translation from Presto to DAGMC. This might be accomplished by eliminating DAGMC's dependence on Cubit.
3. Development of SPH contact algorithms which do not excite hour glass modes of the hexahedral elements would help decrease unrealistic dimples at high pressure interfaces.
4. Development of fluid constitutive response models in Presto which incorporate viscosity and rate dependent terms would enable more accurate predictions
5. Developing DAGMC to be able to handle changing mesh topology would allow use of different death mechanisms in Presto like disconnection of elements on death.
6. Being able to analyze the working fluid's effects on reactivity would make the capabilities of DAGMC fully general for solids and fluids. This is a difficult topology problem which is mathematically ill-posed. It involves taking a very large set of SPH elements and using logic to distinguish whether a given point is a single independent entity, a surface point, or an interior point. Several sets of surface points would have to be isolated and then meshed using a point cloud meshing algorithm. Smoothing of the results may be desirable to make the shape less difficult for the DAGMC algorithms. The surface mesh could then be analyzed in DAGMC. This would require that point 5 above be met because the mesh would be new for every time step as the fluid evolves.

5.7. Impact Modeling Conclusions

The structural analyses presented have been used in DAGMC to demonstrate nuclear reactivity as a function of deformed geometry. The analyses have also been driven to a high level of fidelity for the eighty-five pin reactor presented. This establishes that full scale reactor simulations are possible for current technology. The working fluid has been included using SPH elements. The entire process of building a complex internal enclosure of SPH elements which do not overlap with the surrounding solid surfaces has been developed through a custom Fortran program. Data transmission between DAGMC and Presto is currently a highly manual process which has been presented in detail. Future work needs to be done in order to streamline the one way coupling. In order to make DAGMC fully general for fluids and solids in a reactor, a method for converting an SPH point cloud to a set of surfaces needs to be developed. Several initiatives such as validation of the SPH fluid behavior, development of more advanced constitutive behavior for nuclear fuel and working fluids, and improvements to DAGMC's capability to handle general meshes with changing topology will mature the deformed reactivity analysis field so that it will improve nuclear safety assessments in the future.

6. PRELIMINARY IMPACT REACTIVITY MODELING

T. E. Radel

6.1. Zero Order Modeling of Impact Reactivity Change

6.1.1. 19-pin Rector Studies

The simple 19-pin reactor was used to test the accuracy of the DAGMC conversion process with respect to neutronics. The geometry was also modified to an approximated post-impact configuration. Calculations were performed on all three files (standard MCNP, DAGMC, and approximated post-impact MCNP) with multiple surrounding materials.

As the approach discussed in this paper will ultimately be tested on an 85-pin reactor concept [Marcille 2006], a simplified 19-pin version of this reactor was developed for some initial model testing. Various design parameters are listed in Table 6-1 and the configuration is shown in Figure 6-1 and Figure 6-2. Like the 85-pin reactor, the 19-pin core is in a hexagonal array that is encased by a 12-sided steel baffle. Nineteen homogenous fuel pins contain UO_2 enriched to 93% ^{235}U, SS-316 clad, and Gd_2O_3 poison. The fractions of each material are calculated from Marcille et al [Marcille 2006]. The density of the fuel was artificially increased in the MCNP input file to achieve a k_{eff} of approximately 1 with a 90 degree rotation of the control drums.

Table 6-1. Design Parameters for the 19-Pin Concept.

Parameter	Value
Number of fuel pins	19
Fuel length (cm)	38
Axial reflector length (cm)	2
End cap length (cm)	0.5
Fission gas plenum length (cm)	1
Pin OD (cm)	2.108
Pin pitch	2.372
Fuel pellet OD	1.994
Fuel clad thickness	0.051
Inner basket wall thickness (cm)	0.1
Downcomer thickness (cm)	0.42
Vessel thickness (cm)	0.25
Control drum OD (cm)	8.1
Maximum reflector thickness (cm)	7.7
Water shield OD (cm)	21.46
Inner basket height (cm)	46.5
Vessel height (cm)	52.5
Reflector height (cm)	52.5

Outside of this inner vessel lies a downcomer region, and outside of the downcomer is the 0.25 cm SS-316 pressure vessel. The reactor uses six scaled-down external control drums encased in a cylindrical radial water shield, as depicted in the cross section view in Figure 6-2. The thin B_4C elements of the drums are shown in a “full in” (180 degrees) orientation in this figure, which would be the launch configuration if this were an actual reactor. The remainder of the drum

elements and the interstitial radial reflector are composed of beryllium. The reactor utilizes a borated-water shield contained in a SS vessel.

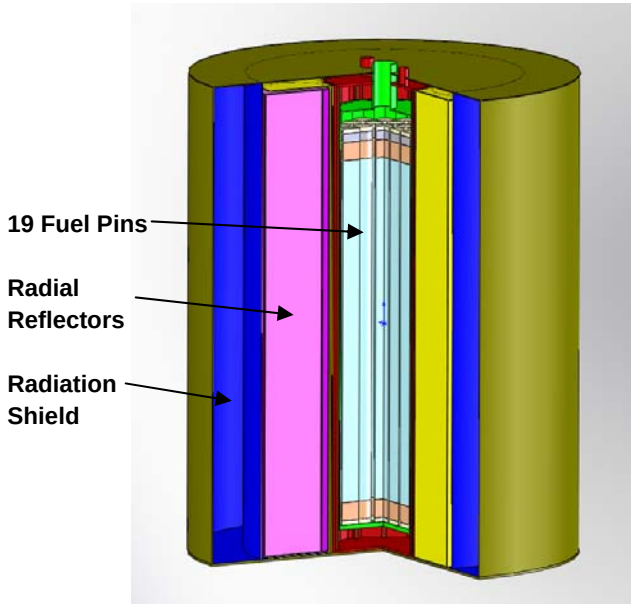

Figure 6-1. 19-pin Reactor Configuration.

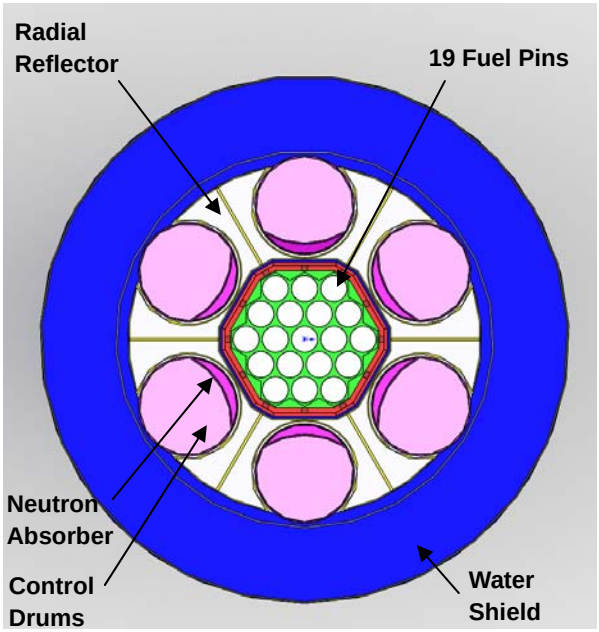

Figure 6-2. Top View of 19-Pin Reactor Cross Section.

An MCNP input file was created by hand for the geometry described above. A commonly used measure of how close a reactor is to a critical state with a self-sustaining chain reaction is the neutron multiplication factor k-effective, or k_{eff}. It is the ratio of the number of neutrons produced in each succeeding generation of absorption and fission (with typically about two new

neutrons produced per fission). A k_{eff} = 1.0 means that the chain reaction is exactly balanced and the reactor power is neither increasing nor decreasing. The reactor "reactivity" is the deviation from k_{eff}, normalized by k_{eff}:

$$\rho = \frac{k_{eff} - 1}{k_{eff}} = 1 - \frac{1}{k_{eff}} \tag{6-1}$$

The k_{eff} with the control drums at 180 degree, full in, was 0.94119 with a standard deviation of 0.00092. The result with the control drums at 0 degrees, full out, was a k_{eff} of 1.02440 with a standard deviation of 0.00110. (See Table 6-2).

To compare these standard MCNP results with results obtained using DAG-MCNP5, the geometry (with control drums full in) was modeled in SolidWorks 2009 and then imported into Cubit 10.2. Overlapping and duplicate surfaces were removed and a region of zero importance which bounded the problem was created. Material properties were also assigned within Cubit. The geometry was then exported as an ACIS geometry file and run with DAG-MCNP5. The results were a k_{eff} of 0.94095 with a standard deviation of 0.00092.

Inspection of the FEA results for the 19-pin reactor 40-m/s impact (Figure 5-5) suggests that the fuel pins will be deformed in such a way that they will come into contact with neighboring pins in the lower region of the fuel. As a comparison for future DAG-MCNP5 runs with the 19-pin deformed geometry, an MCNP file with an approximated post impact geometry was created. The fuel was deformed such that the pins were just touching one another for the bottom 50% of the fuel. The upper portion of the fuel remained undeformed. The fuel length was shortened to conserve fuel volume. The reflector and control drums region was also shortened and subsequently widened to conserve volume. For a comparison run, the water shield was also shortened. (See Figure 6-3 and Figure 6-4)

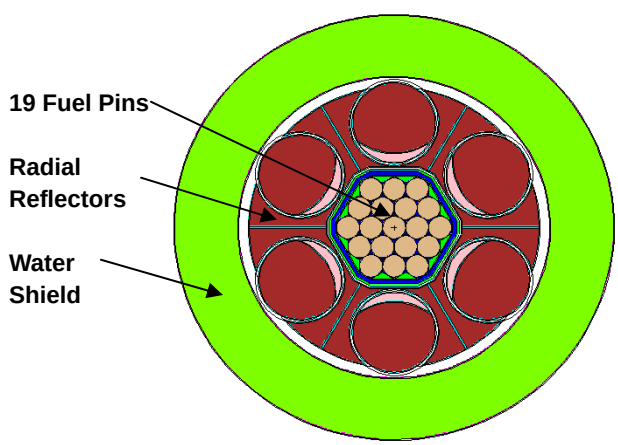

Figure 6-3. Lower Portion Fuel Geometry in 19-Pin Post-Impact Approximated Geometry.

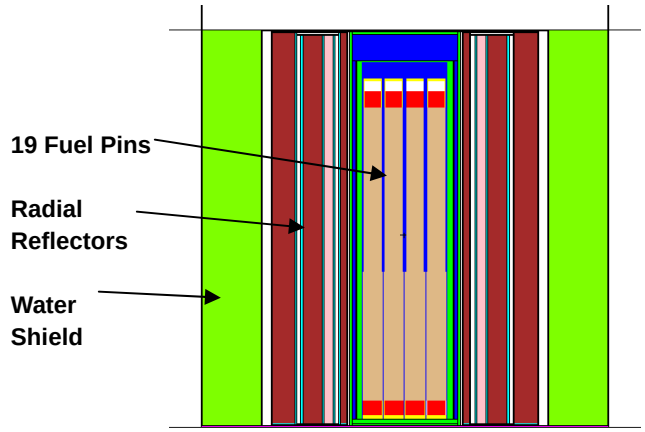

Figure 6-4. Front Cross-Sectional View of 19-Pin Post-Impact Approximated Geometry.

This post-impact approximated geometry was run in various configurations with multiple surrounding materials. A base comparison was done with control drums full in and the water shield still intact. The reflectors, control drums, and water shield were then removed and this vessel only geometry was run with pure water, wet sand, and liquid hydrogen as surrounding materials. The results are shown in Table 6-2. The results for the undeformed geometry were added to the table also, for comparison purposes. For the shutdown condition with the reflectors still present after impact, k_{eff} increased by about 8% (from 0.94 to 1.02). The reactivity increased from -0.06 to +0.02.

Table 6-2. MCNP Results for 19-pin Reactor Model.

Status	Geometry (CD* position)	Surrounding Material	Keff (std dev)
Pre-Impact	Water Shield (0)	Void	1.02440 (0.00110)
Pre-Impact	Water Shield (180)	Void	0.94119 (0.00092)
Post-Impact	Water Shield (180)	Void	1.02292 (0.00098)
Post-Impact	Pressure Vessel (NA)	Water	0.98582 (0.00107)
Post-Impact	Pressure Vessel (NA)	Wet Sand	1.03066 (0.00103)
Post-Impact	Pressure Vessel (NA)	Liquid H_2	0.93010 (0.00101)

* Control Drum, 0 degrees is full out, 180 is full in

The previous results are interesting, but were obtained with a non-physical design that was used primarily to develop the modeling techniques starting with a simple geometry. The density of the fuel in the 19-pin reactor was artificially increased to make the k_{eff} near critical. To determine if the behavior seen in the 19-pin design is still valid for a more realistic design, the 85-pin reactor design of Marcille was run with all the same configurations as the 19-pin reactor runs. Figure 6-5 shows a cross section of the core prior to the impact modifications. Similar to the 19-pin case, the lower 50% of the 85-pin model was modified so that the pins were in contact

with each other. The results can be seen in Table 6-3. For the shutdown condition with the reflectors still present after impact, k_{eff} increased by about 6% (from 0.86 to 0.91). The reactivity increased from -0.16 to -0.10. This is comparable to the 19-pin reactor. But the 85-pin reactor remains subcritical by a substantial margin after impact because it has a lower initial reactivity in shutdown mode. This suggests the need to have a substantial amount of subcriticality for launch. These preliminary scoping calculations also emphasize the need to have a model that can transfer the detailed distorted geometry to a reactivity code so as to achieve a more accurate calculation.

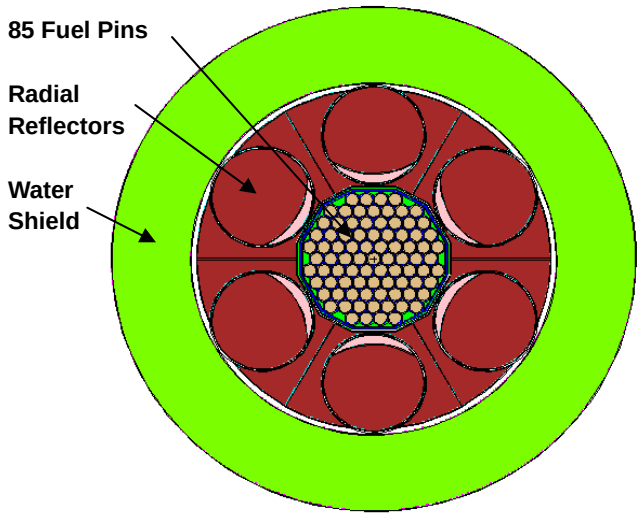

Figure 6-5. Top Cross-Sectional View of 85-Pin, Pre-Impact Geometry.

Table 6-3. MCNP Results for 85-pin Reactor Model

Status	Geometry (CD* position)	Surrounding Material	Keff (std dev)
Pre-Impact	Water Shield (0)	Void	1.02072 (0.00096)
Pre-Impact	Water Shield (180)	Void	0.86142 (0.00101)
Post-Impact	Water Shield (180)	Void	0.90915 (0.00076)
Post-Impact	Pressure Vessel (NA)	Water	0.88644 (0.00105)
Post-Impact	Pressure Vessel (NA)	Wet Sand	0.95541 (0.00098)
Post-Impact	Pressure Vessel (NA)	Liquid H_2	0.81910 (0.00092)

* Control Drum, 0 degrees is full out, 180 is full in.

6.2. Simple Cylinder Modeling with DAGMC

The workflow of the coupled impact simulation and criticality calculation was tested with a simplified problem consisting of a single right circular cylinder (R=12 cm, H=38 cm) of 93% enriched UO_2 (ρ=10 g/cm^3) in a vacuum. A coarse mesh was applied to this geometry (1215 elements in the cylinder).

Table 6-4 shows a summary of results from a simulation using the native geometry format of MCNP5, the solid model-based faceted geometry representation of DAG-MCNP5 (with different faceting approximations), and the mesh-based geometry representation of DAG-MCNP5 for use in this workflow. All cases had 5000 histories per generation with 25 inactive and 100 active cycles. Most apparent in the results is the volume discrepancy among the various geometry representations. It is clear that the different faceting/meshing tolerance results in underestimation of the total volume of fissile material which has an impact on the calculated value of k_{eff}. It will be important to ensure that the meshing is fine enough to provide a good approximation of the volume of each region. The 0.73% missing volume results in a 0.31% underestimation of k_{eff}, a difference of nearly 4σ.

Table 6-4. Results of Test Problem using Different MCNP5 Geometry Representations.

Geometry Representation (Faceting tolerance)	Cylinder Volume [cm3]	Surface Facets (cylinder)	k_{eff} (std dev)
Native	17190.8	9 (3)	0.98373 (0.00080)
Solid Model (10^{-3})	17188.9	1028 (972)	0.98179 (0.00085)
Solid Model (10^{-4})	17190.6	3132 (3076)	0.98363 (0.00100)
Solid Model (10^{-5})	17190.8	9788 (9732)	0.98391 (0.00099)
Mesh	17065.4	9312 (612)	0.98077 (0.00089)

7. ADVANCED IMPACT MODELING WITH DAGMC

B. M. Smith and P. P. H. Wilson

The post-impact deformed geometry determined by the structural analysis code must be input to a neutronics tool capable of predicting reactivity. The deformed geometry is a volume-meshed finite element model. However, Monte Carlo tools use surface-based geometry. This chapter describes the workflow, initialization, and transport algorithms required to adapt deformed mesh geometry for use in Monte Carlo radiation transport. Deformed space reactor analyses are presented to demonstrate the capabilities developed.

7.1. Introduction to DAG-MCNP5

The Monte Carlo N-Particle (MCNP) radiation transport code was selected to determine the reactivity of the nuclear system [Breismeister 1997]. Applications exist to support the use of CAD geometry in MCNP [Wu 2007, Schwartz 2005, White Rock 2010, Wang 2005, Sato 2006, Tsiege-Tamirat 2005, Raytheon 2010, Caracappa 2005, and Tautges 2009]. These can be grouped into either the *translation* approach or the *direct* approach. In the translation approach, CAD geometry is converted to MCNP's native geometry of first and second order analytic surfaces. The direct approach alters MCNP such that geometric queries are performed on the CAD geometry itself. Neutronics modeling of deformed geometry is best performed by the direct approach because the exact deformed geometry is retained.

One implementation of the direct approach is Direct Accelerated Geometry Monte Carlo (DAGMC) software library, developed at the University of Wisconsin [Tautges 2009]. Referred to as DAG-MCNP5 when coupled with MCNP5, it has been used for many fusion and fission applications featuring complex CAD geometry [Sawan 2008]. DAGMC uses the Mesh Oriented datABase (MOAB) for efficient geometric queries on meshed models [Tautges 2004]. The Common Geometry Module (CGM) is used by MOAB to perform geometric queries on solid models [Tautges 2001]. Together CGM and MOAB enable DAGMC to perform ray casting inside solid or faceted CAD models. In this work, finite element mesh models are initialized to create DAGMC-compatible faceted models.

7.1.1. Unique Challenges of Deformed Geometry

During impact, mesh elements may experience structural forces that result in fracture. Mesh elements lose their stiffness to simulate fracture, and are labeled as *dead*. When declared dead, elements cease to participate in the remainder of the structural analysis. Adjusting the mesh topology to removed dead elements requires special treatment.

Fluid volumes are not explicitly meshed and modeled in the structural analysis. DAGMC has the ability to implicitly define void space, known as the *implicit complement*. This is a useful feature because MCNP requires that all space be defined in volumes. The implicit complement allows structural components to deform around fluid components of the model without requiring additional geometry definition in the solid, meshed, and deformed models.

Structural analysis with contact requires adjustments to the particle tracking algorithm. The contact algorithm of the structural analysis permits small overlaps between adjacent bodies. When initialized for DAGMC, small overlaps result in self-intersecting volumes. Common point

membership tests fail for self-intersecting volumes. Small overlaps are problematic for particle tracking because the next surface intersection may exist slightly behind the particle's geometric location. Although overlaps are small enough not to affect the physics of the simulation, additional logic is required for successful particle tracking.

7.1.2. Deformed Geometry Workflow

A solid model of the reactor geometry is created in any format that the Cubit geometry and mesh generation toolkit can import [Sandia 2010]. The solid model is meshed in Cubit. Structural components are meshed with hexahedra. Optionally, fluid volumes are filled with smoothed particle hydrodynamics (SPH) elements. The mesh is exported from Cubit to a structural analysis code using the Exodus II file format [Schoof 1994]. The output of the structural analysis is an Exodus II formatted file of the deformed mesh.

The Exodus II output file alone is not sufficient to perform a DAG-MCNP5 analysis. Additional geometry must be specified to define reflective and absorbing boundary conditions around the deformed model. Boundary conditions and materials are specified by assigning groups to the solid model within Cubit. An MCNP5 input file is created with material definitions and other data cards, but no cell or surface cards. The MCNP5 input file, Cubit geometry file, and Exodus II deformed mesh file are needed to perform a reactivity analysis.

7.2. Geometry Initialization

The geometry initialization is performed with a single executable. No manual model manipulation is required. Cubit files contain both solid and mesh entities, while the Exodus II file only contains mesh entities with deformation. A geometry initialization routine is used to build a geometry input file for DAG-MCNP5 with the following steps:

1. Read solid and mesh model from Cubit file.
2. The surfaces of the solid model are faceted into triangles and associated with the corresponding surfaces of the mesh model. Corresponding geometric entities have the same global IDs.
3. A uniform surface sense is created for each pair of corresponding solid/mesh surfaces. This ensures that corresponding surfaces of the solid and mesh models have the same orientation.
4. The Exodus II deformed mesh file is read. An association between nodes in the Cubit file and Exodus II file is created. Node Ids must be the same in both files to robustly associate nodes pre/post deformation.
5. Node coordinates of the mesh model are updated with deformed locations from the Exodus II file.
6. Dead mesh elements are removed from the mesh model.
7. The bounding faces of the mesh model are found by skinning the mesh model. Skinning is the process of determining the lower-dimensional boundary of a collection of mesh entities. The bounding faces have been altered by the removal of dead mesh elements. The mesh surfaces are updated for topological changes, and new surfaces are created for mesh faces that do not belong to previously existing surfaces of the mesh model.

8. If corresponding surfaces exist, surfaces of the solid model are replaced by surfaces of the mesh model. This preserves surfaces of the solid model belonging to boundary conditions that do not exist in the mesh model, including reflecting and absorbing boundaries.
9. Quadrilateral elements are converted to triangles by splitting along the shortest diagonal.
10. Surfaces are removed if they no longer contain any mesh faces. Volumes are removed if all of their surfaces have been removed.
11. The density of each volume is adjusted so that mass is conserved through the deformation. Volumes of structural components may change due to element death and material compressibility. The solid model with a facet tolerance of 0.0001 cm is used to determine the undeformed volume.
12. Write MOAB-formatted output file for DAGMC.

To illustrate the DAGMC initialization, Figure 7-1 shows two states of a single volume. The volume is a structural steel component in the 85-pin 0-degree model that included SPH elements. Figure 7-1a shows the Cubit hexahedral mesh as input to the structural analysis. Figure 7-1b shows the deformed geometry as initialized for DAGMC. The nodes are matched (Step 4) then moved (Step 5). Dead elements have been removed, leaving a void (Step 6). A new surface (yellow) has been created with mesh faces exposed by removing dead elements (Step 7). Quadrilateral mesh faces are converted to triangles (Step 8).

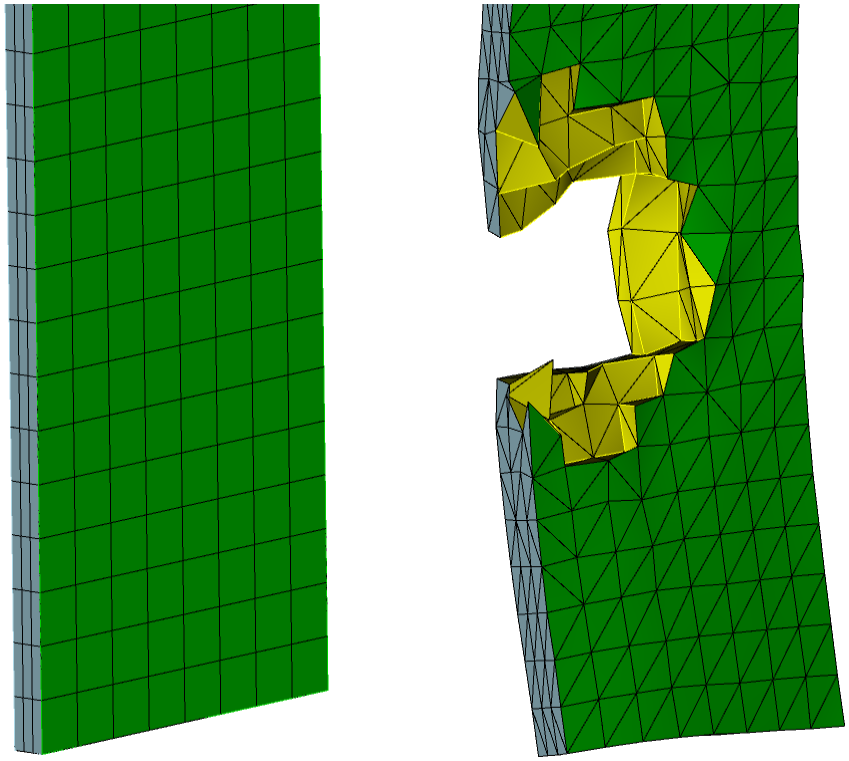

a. b.

Figure 7-1. Undeformed Cubit Mesh (a) and DAGMC Geometry at 0.225 ms (b).

7.3. Particle Transport

In a well-posed DAGMC geometry, surfaces are assumed to be neither coincident nor overlapping. This assumption is not true for deformed structural models, which include small overlaps due to contact from adjacent volumes. A point membership test is used to determine the volume that source particles start inside. Because the existing test in DAGMC is not tolerant of self-intersecting volumes, a new point membership test was developed. After source particles are born, an algorithm is needed to track particles through collisions and surface crossings until they are removed from the simulation. An overlap-tolerant particle tracking algorithm was developed to find surface intersections, even if the next surface is behind the particle's current location. This new functionality is required when using deformed geometry in DAGMC. In addition, it enables CAD models that contain small overlaps to be analyzed in DAGMC without manual repair of the solid model. Avoiding manual CAD repair significantly reduces the time required to perform an analysis.

7.3.1. Geometric Model

The geometric model created by the initialization routine is in the form of a boundary representation. The solid model consists of geometric volumes, surfaces, curves, and vertices. Geometric entities are represented by meshed entities, including elements, faces, edges, and nodes. DAGMC only utilizes volumes and surfaces. Volumes are represented by their bounding surfaces. Surfaces are represented as sets of mesh faces. Mesh faces are triangles specified by three nodes. Individual mesh faces and their geometric surface share the same orientation. The boundary of each volume is a manifold. However, surfaces may be shared by two volumes, creating a non-manifold model. After deformation the boundary of a volume may contain self-intersections due to imprecise contact calculation of the impact code. An exaggerated illustration of a self-intersecting volume is shown in Figure 7-2. Self-intersections can also be caused by imperfect draftsmanship and file translation of a solid model. These errors are tedious to repair, requiring extensive manual labor. The ability to perform particle transport through geometry with small defects will enable deformed mesh analysis and accelerate traditional solid model analysis. The remainder of this section discusses new methods to support point membership testing and particle tracking through volumes with self-intersections.

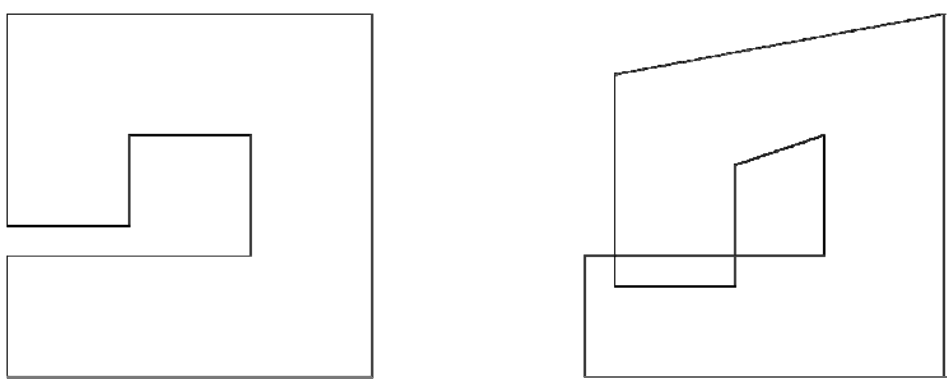

a. b.

Figure 7-2. 2-D Volume before (a) and after (b) Impact.

7.3.2. Point Membership Test

Given a point and volume, the point membership test returns *inside*, *outside*, or *on boundary*. DAGMC originally uses the enlarged orientation method to determine point membership of polyhedral volumes [Horn 1988, Nordbeck 1967, Khamayseh 2008]. In this method, the closest location to the point is found on the boundary of the volume. The closest location may occur inside a triangle, inside an edge, or on a node. If the closest location is on the interior of a triangle, the triangle normal vector is compared with a vector from the point to the closest location on the boundary. If the dot product of the vectors is positive, the point is inside the volume. If the closest location is on an edge or node between two or more triangles, the neighborhood of adjacent triangles must be inspected. The adjacent triangle normal vectors are compared with the point to determine if the edge or node is a local concavity or convexity with respect to the boundary of the volume. The closest location on the boundary can be found using an oriented bounding box (OBB) tree, accelerating an $O(n)$ search to as few as $O(\log n)$ queries. Recent work by Khamayseh and Kuprat demonstrates that a more efficient test is possible by using the closest location on the boundary in any single direction instead of the closest location on the boundary in all directions [Khamayseh 2008].

Figure 7-3a shows the enlarged orientation method applied to a self-intersecting volume in 2-D. Four points are labeled A-D. Each point is drawn with a vector to the closest location on the boundary of the volume. The point is inside if the vector to the closest location and the surface normal vector point in the same direction. Table 7-1 shows the result of the enlarged orientation method for points A-D. Incorrect results are in parentheses. The enlarged orientation method determines point C to be outside because the surface normal vector of the closest location has opposite orientation due to overlap.

Table 7-1. Results of Point Membership Test

Method	Point A	Point B	Point C	Point D
Enlarged Orientation	In	Out	(Out)	In
Ray Crossing	In	Out	In	(Out)
Ray Crossing w/ Orientation	In	Out	In	In
Winding Number	In	Out	In	In

An alternative point membership test is the ray crossing method [Nordbeck 1967]. A ray is cast from the point in any direction. If the number of surface intersections is odd the point is inside the volume. Although they occur infrequently, intersections with edges or nodes of the polyhedral boundary must be further inspected using the neighborhood of adjacent triangles. The computational expense of determining every intersection with a ray increases with the complexity of the boundary. Figure 7-3b illustrates the ray crossing method for points A-D, with results listed in Table 7-1. The ray crossing method fails for self-intersections as indicated by point D. Extra crossings caused by overlaps reverse the even-odd parity of the test, with an even number of crossings (2) incorrectly determining *outside*.

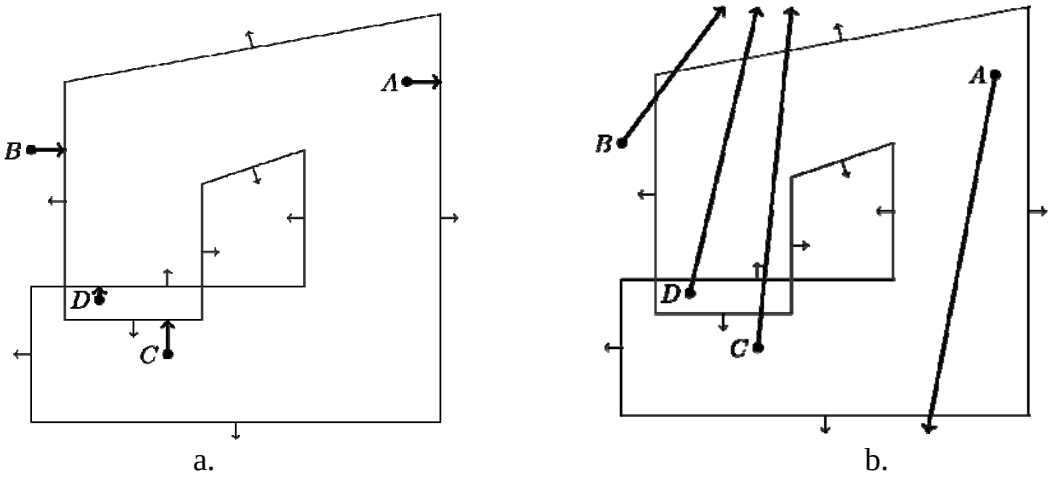

Figure 7-3. Enlarged Orientation (a) and Ray Crossing (b) Methods.

The ray crossing method can be altered to give correct results for self-intersecting volumes. The *ray crossing method with orientation*, as shown in Algorithm 6-1, uses the direction of each crossing to sum the entering/exiting nature of intersections along the ray. The boundary of polyhedral volumes can be decomposed into one or more 2-manifolds. Each point of a 2-manifold has a neighborhood topologically equivalent to a 2-D disk [Bohn 1993]. Figure 7-4 shows two volumes decomposed into 2-manifolds. Thin lines indicate internal voids and their overlaps. Thick lines indicate the volume outer boundary and overlaps of the volume. Figure 7-4a represents an explicitly modeled volume of a structural component that has been deformed due to impact. Figure 7-4b represents an implicitly modeled volume containing fluid. Although the fluid is not modeled as hexahedra in the structural analysis, structural components define its boundaries.

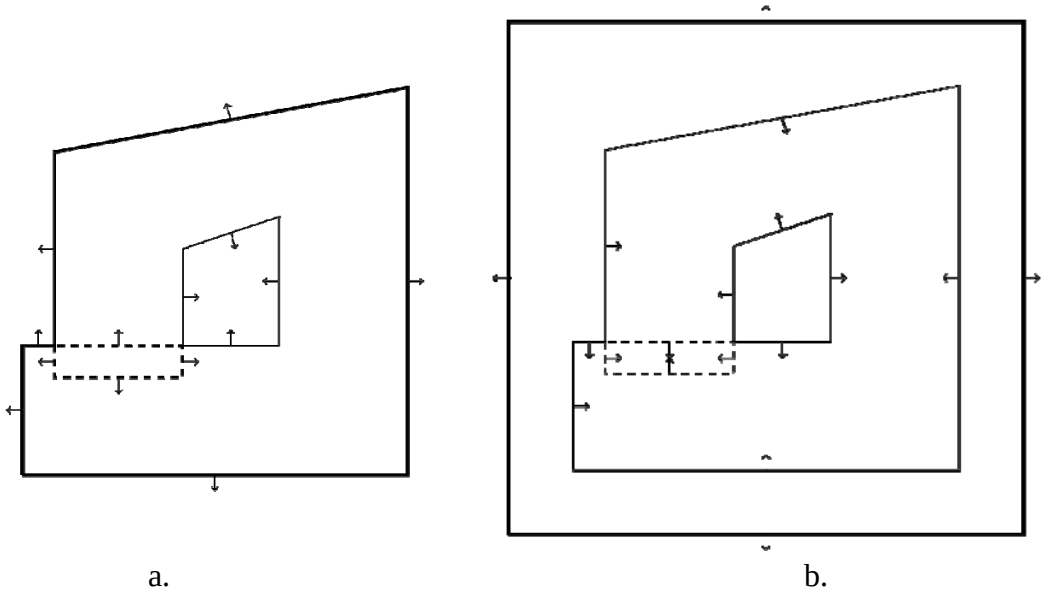

Figure 7-4. Deformed Structural Component (a) and Surrounding Fluid (b) Volumes Decomposed into 2-Manifolds.

Surface orientation can be taken into account to characterize the 2-manifolds, as summarized in Table 7-2. Points inside no manifold have the same number of entrance and exit intersections. Points inside volume overlaps (thick, dashed line) and the volume outer 2-manifold (thick line) are characterized by one more exit than entrance intersection. Points inside internal voids (thin line) and internal void overlaps (thin, dashed line) are characterized by one more entrance than exit intersection. The number of entrances and exits are summed along the ray cast from the test point. *A point that is inside the volume will have at least one more exit than entrance.* Volumes of structural components are explicitly modeled in the structural analysis and only contain volume overlaps. Volumes containing fluid material are not explicitly modeled as hexahedra in the structural analysis and only contain void overlaps. Table 7-1 lists the results of the ray crossing with orientation method on points A-D.

Table 7-2. Surface Crossing Parity of 2-Manifolds.

2-Manifold that Point is Inside:	Number of Entrances	Number of Exits
None	V	V
Volume Outer Boundary	W	W+1
Volume Overlap	X	X+1
Internal Void	Y+1	Y
Internal Void Overlap	Z+1	Z

Care has been taken to minimize numerical error, avoid unnecessary tolerances, and ensure consistency between the point membership test and tracking algorithm. An offset is an optional input to this test, and as later described, the tracking algorithm. The offset allows the same numerical computation to be performed for particle tracking and point membership. This ensures a consistent result for both algorithms, independent of numerical error. A list of previously intersected facets is maintained by the tracking algorithm for each streaming event, and is an optional input to the point membership test. The facet of closest intersection to the point is compared with the list of previously intersected facets. If the closest intersection is a previously intersected facet, the *on boundary* result can be identified.

Algorithm 6-1. Ray Crossing with Orientation

```
point_membership(vol, pt, dir, offset, prev_facets, &result)
   1.  If(NULL == dir) dir = random
   2.  origin = pt – dir*offset
   3.  call ray_cast(vol, pt, dir, &surfs, &dists, &facets)
   4.  for(all dists)
   5.    dists[i] -= offset
   6.    if(0 > dists[i]) dists.erase(i)
   7.  if(!dists.empty)
   8.    min_idx = min_element(dists)
   9.    if(true == find(prev_facets, facets[min_idx]))
   10.     return result = on_boundary
   11. sum = 0
   12. for(all dists)
```

```
  dot_prod = dot_product(dir,facet[i])
  if     (0 < dot_prod) sum += 1
  else if(0 > dot_prod) sum -= 1
if(0 > sum) return result = inside
else        return result = outside
```

For completeness, the winding number point membership test is discussed [Lane 1984]. In this test every facet of the polyhedron is projected onto a unit sphere centered at the point. The projected area is positive if the facet normal vector points away from the point; otherwise negative. If the point is inside the polyhedron, the area of the summed projection will be 4π. If the point is outside, the area will be 0. In a similar observation as used for the ray crossing with orientation method, points within an overlap will have an additional 4π projection. The results of the winding number test on the deformed volume are shown in Table 7-1. Although suitable for overlaps, the winding number test is avoided because it has a time complexity of $O(n)$ where n is the number of facets in the polyhedron.

7.3.3. Tracking Algorithm

The tracking algorithm in DAGMC searches for the intersection at which a particle leaves the current volume, known as the *exit intersection*. After initialization, each surface is adjacent to exactly two volumes. When a particle leaves the current volume, the next volume is determined using surface adjacency information. The tracking algorithm then searches for the exit intersection of the next volume. Only exit intersections are found because the current volume's exit location is identical to the next volume's entrance location.

Self-intersecting volumes present a challenge because the exit intersection may occur behind the particle's geometric location. This allows the geometric and logical position of a particle to come out of sync. Algorithm 6-2 allows the logical location of the particle to be updated without changing the geometric location, bringing the geometric and logical location back into sync. Altering the logical location without a corresponding change in geometric location is valid because the overlap thickness is assumed to be small enough to not significantly affect the physics of the simulation.

Figure 7-5 is an example of a fluid volume with three voids, assumed to be structural components. The particle has entered the volume at *a* and exited at *b*. After traveling through a different volume it again entered at *c* and exited at *d*. After traveling through a different volume it again entered at *f*. The next exit location should be *e*, but *e* is behind the particle's current location. The overlap between *e* and *f* is exaggerated in the figure. If *g* is incorrectly selected as the exit location the particle will become lost because the surface normal is in the wrong direction. If *h* is incorrectly selected as the exit location the particle will never travel through the volume between *e* and *g*.

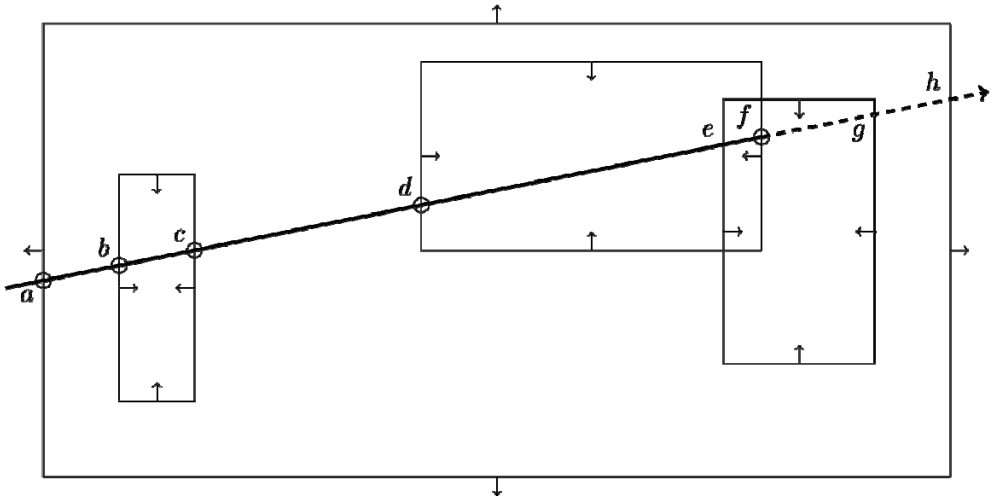

Figure 7-5. Particle Track through a Volume Containing an Overlap.

Algorithm 6-2 describes the process of selecting the correct exit intersection. An exit intersection includes both geometric (location, as a distance) and logical (surface and facet) information. Streaming is significant because a streaming particle will never intersect the same facet twice. This property does not apply to surfaces because surfaces are not typically planar. A list of previously intersected facets is maintained for each streaming event. The algorithm prevents the use of previously intersected facets as exit intersections, to avoid infinite loops in which a particle alternates between exit intersections in close proximity. If a particle intersects a reflecting boundary, only the facet on the boundary is stored.

The distance searched behind the particle for intersections is called the *offset*. The offset is the only tolerance of the tracking algorithm. Particles traveling nearly tangent to an overlap require a large offset. At minimum, the offset is greater than the largest overlap that occurs in the geometric model. In this work 1 cm was used. Increasing the offset reduces the chance of losing a particle, but increases the computational cost of the query. The ray_cast call returns all intersections with correct orientation. An OBB tree is used to accelerate the ray_cast function [Tautges 2009].

Several possible intersections are returned from the ray_cast function. The remainder of the algorithm disambiguates these to determine the correct intersection. The offset is subtracted from the distance of each intersection. The least positive and negative intersections are determined. If the least negative intersection is closer than the least positive intersection and has not been previously intersected, a point membership test is performed. The point membership test ensures that intersections at negative distance are accepted only if located inside an overlap.

The point membership test will return a consistent result because it performs the same numerical ray casting computation. The consistency between the tracking algorithm and point membership test occurs when the particle is at the same geometric and logical location, traveling in the same direction. It does not occur between particle advances due to the numerical error caused by moving the geometric location.

In Figure 7-5, the particle is currently located at *f*. The ray_cast function will return *e* and *h* as possible intersections. Intersections *a*, *b*, *c*, and *d* are not returned because they are in the list of

previously intersected facets. Intersection *g* is not returned because it does not have correct orientation. A point membership test is performed on *f* to make sure that it is located inside the volume adjacent through the surface of *e*. This is true. *e* is accepted as the next intersection because the magnitude of the distance from *f* to *e* is less than from *f* to *h*. To conserved track length, negative distances are reported to the physics code as zero distance.

Algorithm 6-2. Overlap-Tolerant Particle Tracking

```
track(vol, last_surf_hit, pt, dir, &prev_facets, &d_traveled, &next_surf_hit)
  1.  // reset previous facets if needed
  2.  if(last_surf_hit is reflecting)
  3.    last_facet = prev_facets.back
  4.    prev_facets.clear
  5.    prev_facets.push_back(last_facet)
  6.  else if(particle is not streaming)
  7.    prev_facets.clear
  8.  // perform the ray-cast
  9.  offset = constant_parameter
  10. origin = pt – dir*offset
  11. call ray_cast(vol, pt, dir, &surfs, &dists, &facets)
  12. // get the negative and positive intersections closest to zero
  13. least_pos_dist = double::max, least_neg_dist = -double::max
  14. least_pos_idx = -1, least_neg_idx = -1, exit_idx = -1
  15. for(all dists)
  16.   dists[i] -= offset
  17.   if(0 <= dists[i])
  18.     if(least_pos_dist>dists[i]
  19.     && false==find(prev_facets, facets[i]))
  20.       least_pos_dist = dists[i]
  21.       least_pos_idx  = i
  22.   else
  23.     if(least_neg_dist<dists[i])
  24.       least_neg_dist = dists[i]
  25.       least_neg_idx  = i
  26. if(-1!=least_neg_idx
  27.   && true==find(prev_facets, facets[least_neg_idx]))
  28.   least_neg_dist = -double::max
  29.   least_ned_idx  = -1
  30. // check to ensure the negative intersection is due to an overlap
  31. if(-1!=least_neg_idx && -least_neg_dist<least_pos_dist)
  32.   call next_volume(vol, surfs[least_neg_idx], &next_vol)
  33.   call point_membership(next_vol, pt, dir, offset, prev_facets,
      &result)
```

```
  if(inside == result) exit_idx = least_neg_idx
if(-1==exit_idx) exit_idx = least_pos_idx
// return the next exit intersection
next_surf_hit = surfs[exit_idx]
prev_facets.push_back(facets[exit_idx])
if(0 > dists[exit_idx])
  d_traveled = 0
else
  d_traveled = dists[exit_idx]
```

7.4. Reactivity Calculations

7.4.1. Incremental Development

The geometry initialization and particle tracking routines required substantial changes to support deformed mesh geometry. An incremental approach was taken to development, beginning with a single deformed cylinder of fuel. The deformed cylinder of hexahedral elements (described previously in Figure 5-1) was used to test MOAB's Cubit and Exodus II file reading capabilities, and structure the correspondence between solid, mesh, and deformed models. The entity count and tracking rate of each model is shown in Table 7-3. Entity count includes geometry required for boundary conditions. In general, the particle tracking rate decreases as model complexity increases.

Next a single fuel pin was deformed, with separate volumes for fuel, fission gas gap, shields, and end caps. Cladding was modeled using 2-D shell elements to reduce the computation time of the structural analysis. However, MCNP requires that mass be represented with 3-D volumes. Special treatment is needed for shell elements due to this incompatibility. An initial plan was to homogenize the cladding material with the fuel, yet use the geometry of the shell elements to separate the *fluid* volumes for fission gas and reactor coolant. This approach was unsuccessful because fracture of the cladding unites the coolant and gas volumes, into a single non-manifold volume. The particle tracking algorithm cannot follow particles through non-manifold volumes. For this reason it was decided to avoid shell elements in the structural analysis.

A single fuel pin was deformed without shell elements, reducing the number of triangles. The fuel was modeled with separate fuel pellets, allowing surfaces of adjacent fuel pellets to contact. The transport algorithm was altered to be tolerant of coincident and slightly overlapping surfaces. Dead mesh elements were removed from the geometry. Volume occupied by dead elements was added to the implicit complement. Fluids were combined into the implicit complement volume, and assumed to be void. This allowed development to continue without resolving the mixing fluid dilemma created by fractured structural components.

The next model contained five fuel pins with pellets and cladding meshed with hexahedral elements. This was the last opportunity to test workflow, debug code, and improve the tracking algorithm before larger models made manual inspection and manipulation difficult. As with future models, only a single fluid material that occupies the outside environment, coolant, fission gas gap can be used in the radiation transport simulation. It is likely that the fluid boundaries have been breached, creating a single *mixed* fluid volume.

Table 7-3. Summary of Models Used for Development of Workflow and Tracking Algorithm.

Model	Shell Elems.	Fuel Pellets	Entity Count				Tracking Rate [Part./Min.]
			Vols.	Surfs.	Hex.	Tris.	
Cylinder	No	No	4	25	3161	9312	453760
1-Pin	Yes	No	15	62	110K	167K	232770
1-Pin	No	Yes	32	111	103K	65K	299200
5-Pin	No	Yes	256	841	204K	542K	47501

7.4.2. Comparison of Native and CAD Geometry

Significant changes have been made to the tracking algorithm and point membership test to support deformed geometry. A comparison was performed between native MCNP5 and the newly developed version of DAG-MCNP5. An 85-pin space reactor was analyzed with control drums rotated for minimum neutron absorption. The native geometry is shown Figure 7-6a and Figure 7-6b. Using the MCNP2CAD automated conversion utility, MCNP native geometry was converted to ACIS-formatted CAD geometry as shown in Figure 7-6c. Material properties and boundary conditions were automatically mapped to the CAD file. The model has 1176 volumes and 4947 surfaces. Merging of coincident surfaces in the CAD model was not required due to the overlap-tolerant tracking algorithm. Manual model manipulation was not required. All cases had 10 inactive cycles, 100 active cycles, and 10,000 source neutrons per cycle. No particles were lost. The facet tolerance is the maximum distance between the faceted surface and the continuous surface of the solid model. The neutron multiplication factor of the native geometry is closest to the case with the smallest facet tolerance. Results are shown in Table 7-4.

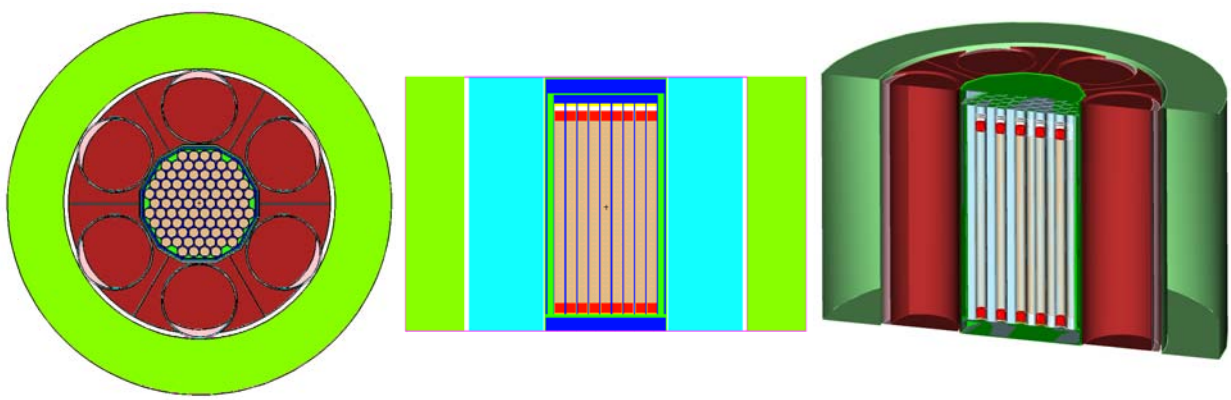

a. b. c.

Figure 7-6. Native MCNP (a,b) and Converted CAD Geometry (c).

Table 7-4. Results of 85-pin Comparison between Native MCNP5 and New Version of DAG-MCNP5.

Geometry Representation	Facet Tol. [cm]	Triangles	K_{eff} (std. dev.)
Native	-	-	1.01437 (0.00075)
Solid Model	0.01	443346	1.01508 (0.00073)
Solid Model	0.001	540666	1.01321 (0.00080)
Solid Model	0.0001	1682678	1.01451 (0.00080)

7.4.3. 85-Pin Reactor Impact Simulations

Three simulations were performed of the 85-pin reactor impacting concrete at 100 m/s. Control drums were rotated to the position of maximum neutron absorption. 0-degree and 45-degree collisions were modeled with neither structural nor reactivity analyses including fluids. To add the effect of fluids, a 0-degree collision was modeled using SPH elements in the structural analysis. Although DAGMC cannot utilize SPH elements, adding fluids increases the accuracy of the impact simulation. The computational time required for structural analysis was decreased by doubling the thickness of the cladding to 0.1 cm. Material density was adjusted to conserve mass in every volume, despite element volume change and the removal of dead elements.

Table 7-5 shows the geometric detail of 85-pin reactor models used for impact simulations. The volume, surface, and triangle count are from the last time step of the DAGMC-initialized geometry. The hexahedra count references the Cubit mesh because hexahedra do not exist in the DAGMC-initialized geometry. Selected time steps for each model were analyzed as a series of DAG-MCNP5 cases. The particle tracking rate is representative of one core on a 2.66 GHz Core2 processor and has been averaged for all cases. Each neutronics case had 10 inactive cycles, 100 active cycles, and 10,000 source neutrons per cycle.

Table 7-5. Summary of 85-Pin Reactor Impact Models.

Angle [Deg.]	SPH	Symmetry	Entity Count				Tracking Rate [Part./Min.]
			Vols.	Surfs.	Hex.	Tris.	
0	No	1/12	1308	6673	962K	1.43M	3793
0	Yes	1/12	3181	17867	966k	1.51M	3137
45	No	½	3176	11729	8.86M	11.1M	2741

7.4.3.1 0-Degree Impact

The 0-degree impact model featured 1/12 symmetry as shown in Figure 7-7a. The criticality of the deformed reactor was investigated at 0.15 ms intervals until all of the kinetic energy had been dissipated. Each DAG-MCNP5 case required 5 hours on one core of a 2.66 GHz Core2 processor. The last time step is shown in Figure 7-7b, occurring at 1.5 ms. The distance between fuel pins decreased as fuel relocated toward the bottom of the reactor. Figure 7-8 shows the node displacement and number of dead elements as a function of time. Dead elements indicate fracture of reactor components. As indicated in Figure 7-9, the neutron multiplication factor (k_{eff}) increased approximately 0.07. Error bars represent one standard deviation. The average lost particle fraction was 4.1×10^{-6}.

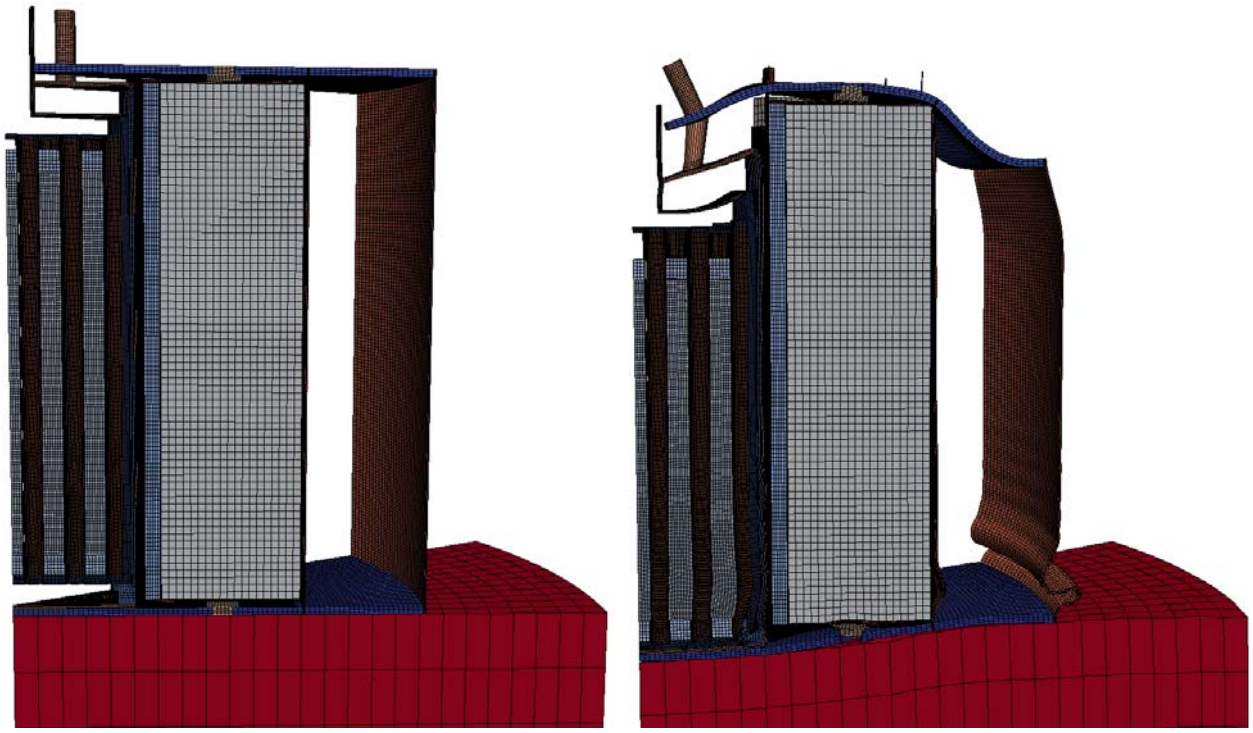

a. b.

Figure 7-7. 0-degree Impact at 0 ms (a) and 1.5 ms (b).

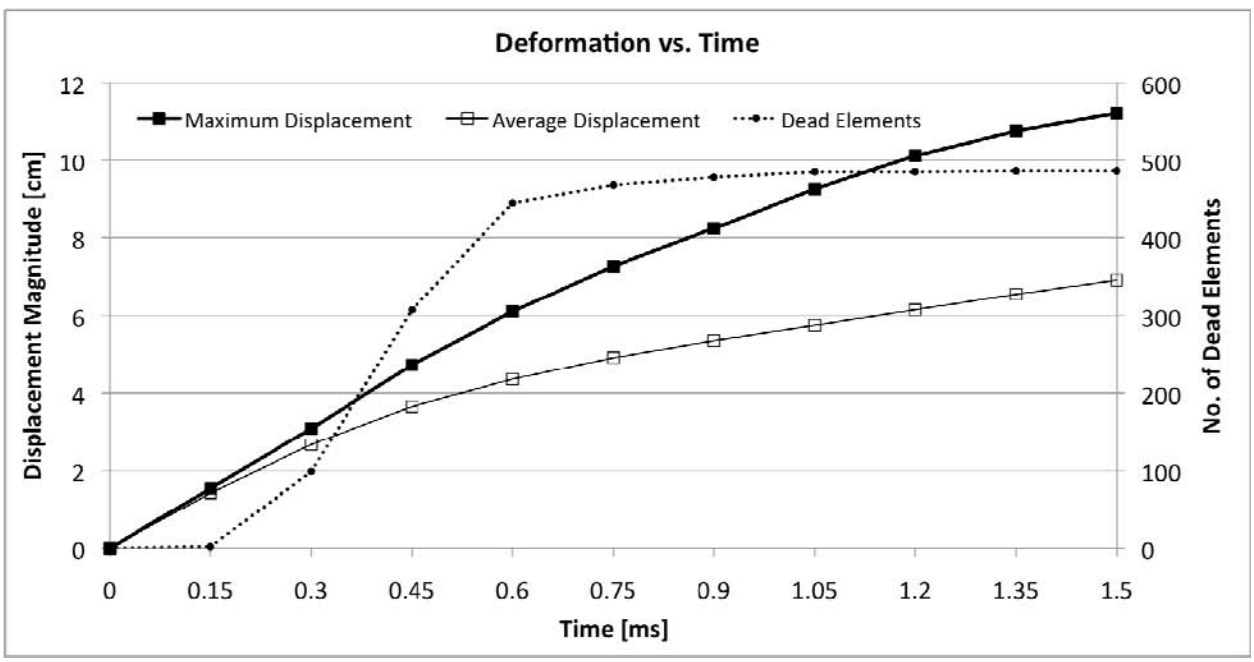

Figure 7-8. Node Displacement and Number of Dead Elements during 0-Degree Impact.

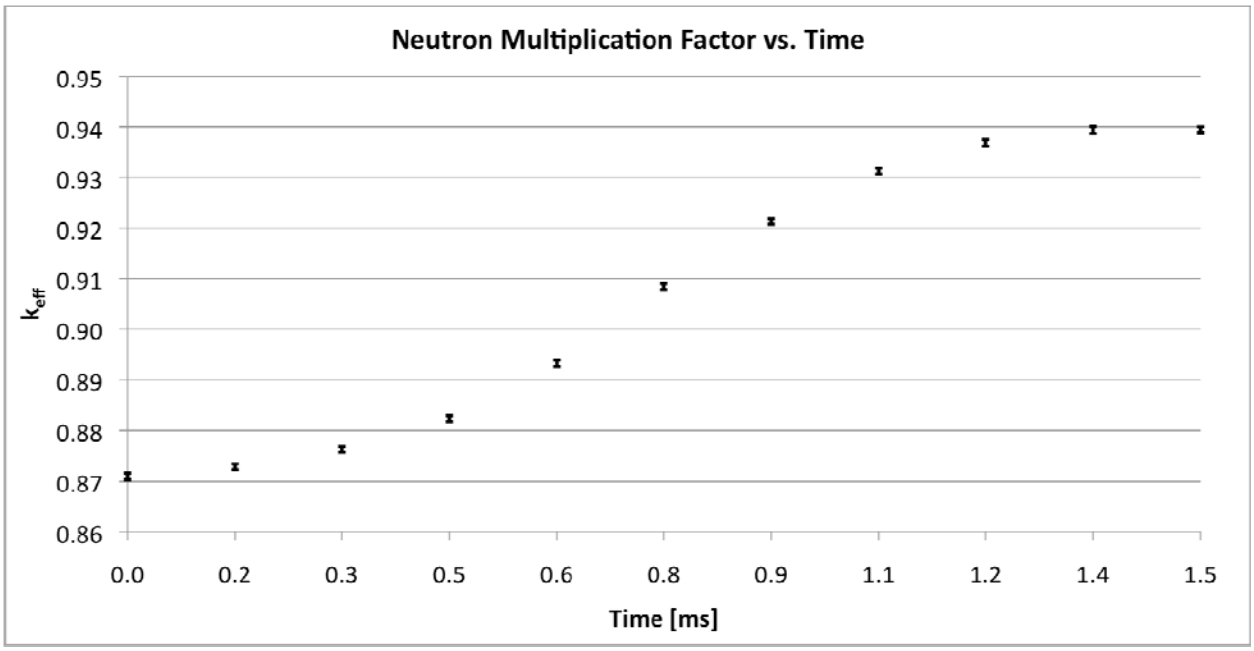

Figure 7-9. Neutron Multiplication Factor during 0-Degree Impact.

Water shielding and NaK coolant were added to the undeformed solid model to determine the effect of neglecting fluids in the reactivity analysis. The neutron multiplication factor increased from 0.87112 (0.00069) to 0.87987 (0.00064) when fluids were included. This suggests that for the 85-pin model, neglecting fluids in the reactivity analysis decreases the neutron multiplication factor ~0.01.

7.4.3.2 0-Degree Impact with SPH Elements

Fluids were included in the structural analysis of a 0-degree impact using SPH elements. As shown in Figure 7-10b, green SPH elements simulate water shielding. Orange SPH elements simulate NaK coolant. The analysis without SPH elements in Figure 7-10a provides a side-by-side comparison at 1.5 ms. Water SPH elements cause the shield containment to break. The NaK SPH elements keep adjacent fuel pins from contacting each other in the radial direction.

At the time of this work, SPH elements were not supported in DAGMC. When initializing geometry from the structural analysis the SPH elements were ignored. The result is a DAGMC-initialized geometry without fluids. Each DAG-MCNP5 case required 6 hours on one core of a 2.66 GHz Core2 processor. Figure 7-11 shows the node displacement and number of dead elements as a function of time. As indicated in Figure 7-12, the neutron multiplication factor increased approximately 0.025. The inclusion of fluids in the structural analysis limited the increase of the neutron multiplication factor, as seen by comparing Figure 7-9 and Figure 7-12. Error bars represent one standard deviation. The average lost particle fraction was 1.3×10^{-6}.

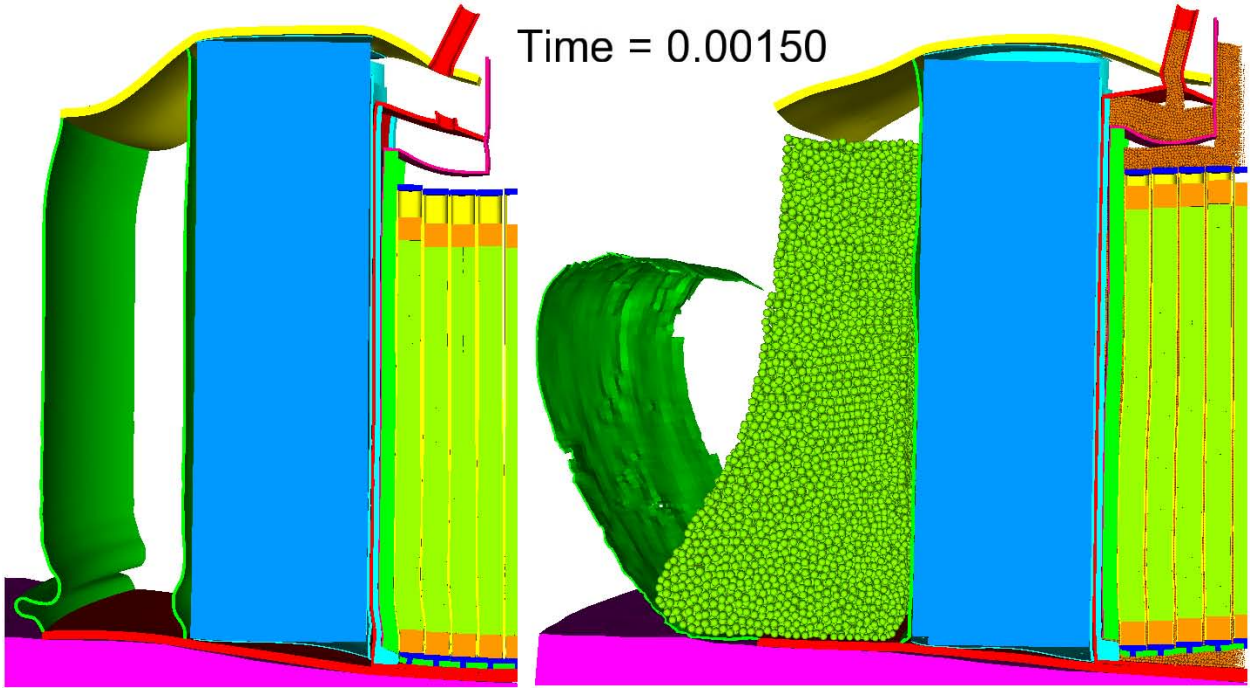

a. b.

Figure 7-10. 0-Degree Impact at 1.5 ms without (a) and with (b) SPH Elements.

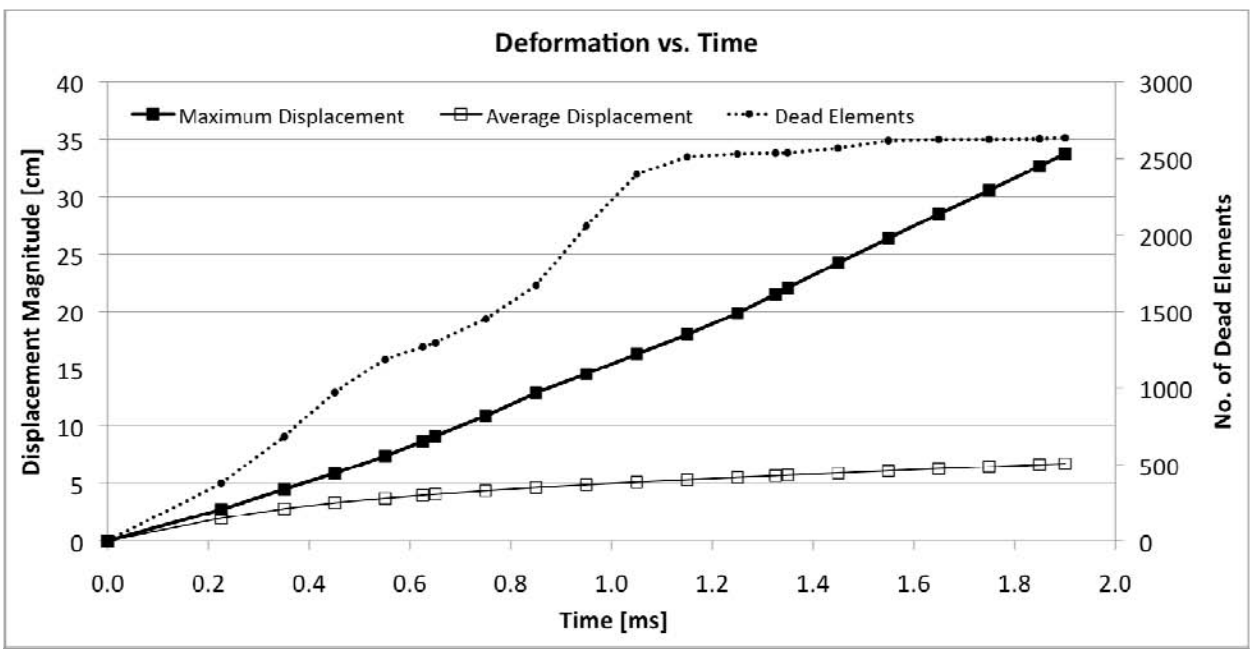

Figure 7-11. Node Displacement and Number of Dead Elements during 0-degree Impact, with SPH Elements in Structural Simulation.

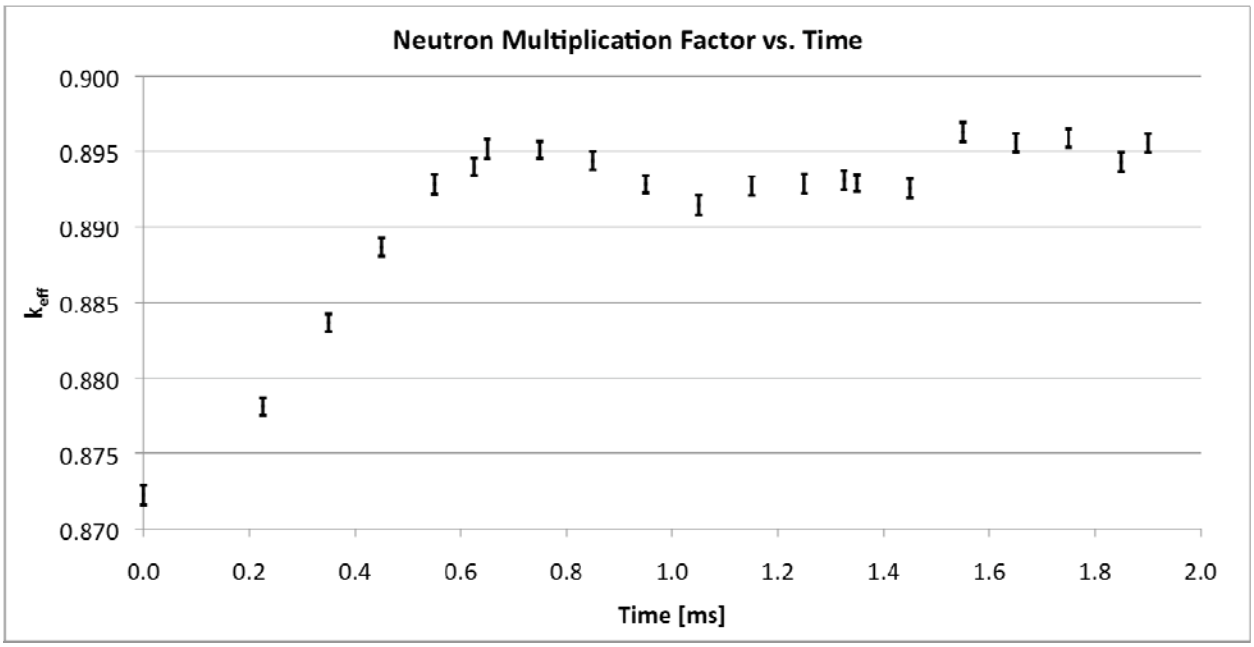

Figure 7-12. Neutron Multiplication Factor during 0-Degree Impact, with SPH Elements in the Structural Simulation.

7.4.3.3 45-Degree Impact

The 45-degree impact model featured 1/2 symmetry. The impact simulation ended at 2.1 ms, as shown in Figure 7-13. Spikes from the top of the reactor in Figure 7-13b are non-physical and result from ParaView showing dead elements in the visualization. Although the simulation was not extended until all kinetic energy was dissipated due to time constraints, it clearly demonstrates the predictive capability. Each case required 7 hours on one core of a 2.66 GHz Core2 processor. Figure 7-14 shows the node displacement and number of dead elements as a function of time. The neutron multiplication factor did not increase for the first 0.95 milliseconds of impact because the fuel pins did not move relative to one another. After 0.95 milliseconds the distance between fuel pins began to decrease with a corresponding increase in the neutron multiplication factor, as shown in Figure 7-15. Error bars represent one standard deviation. The average lost particle fraction was 4.4×10^{-6}.

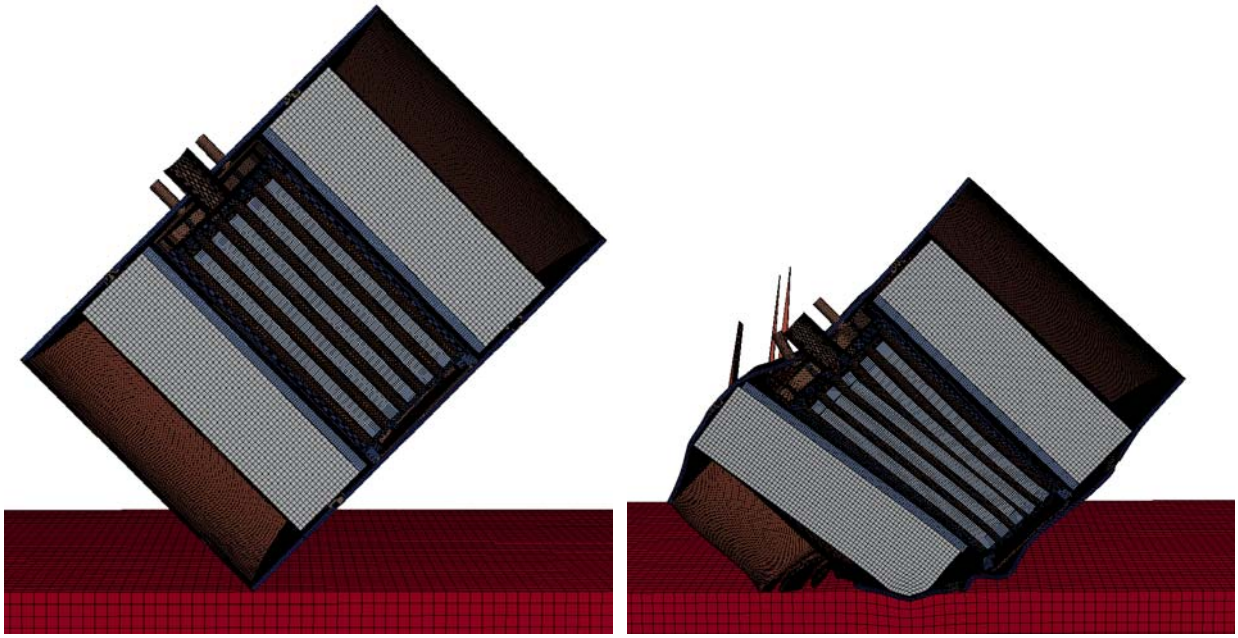

a. b.

Figure 7-13. 45-Degree Impact at 0 ms (a) and 2.1 ms (b).

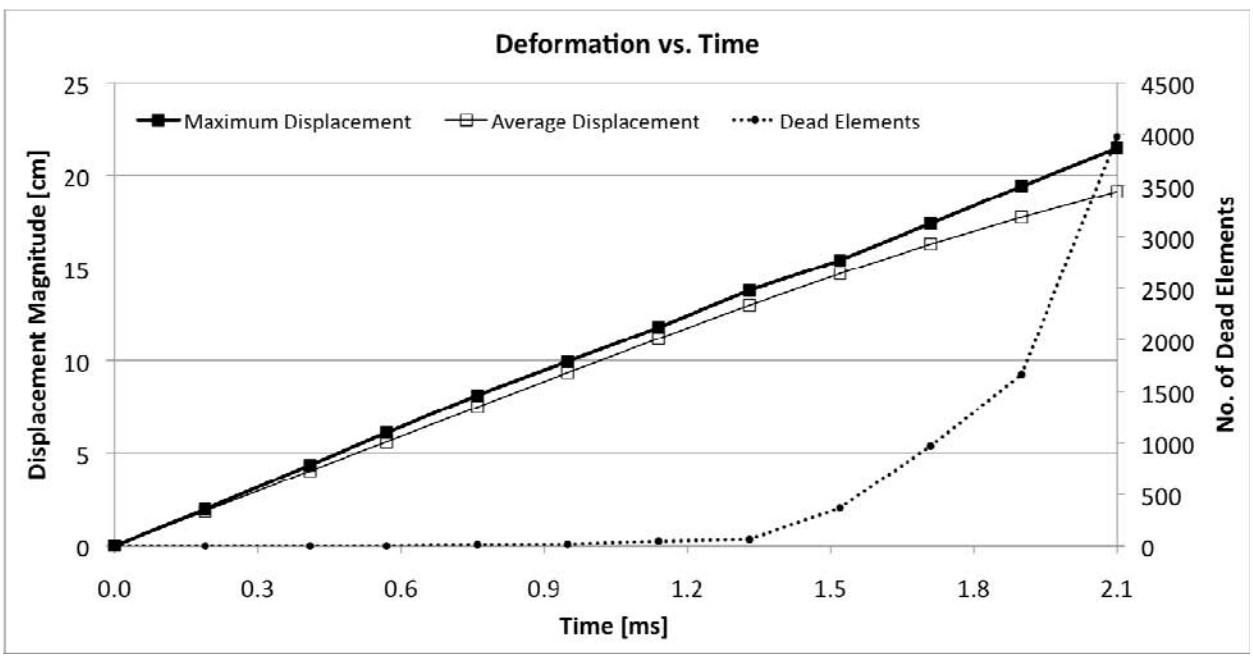

Figure 7-14. Node Displacement and Number of Dead Elements during 45-Degree Impact.

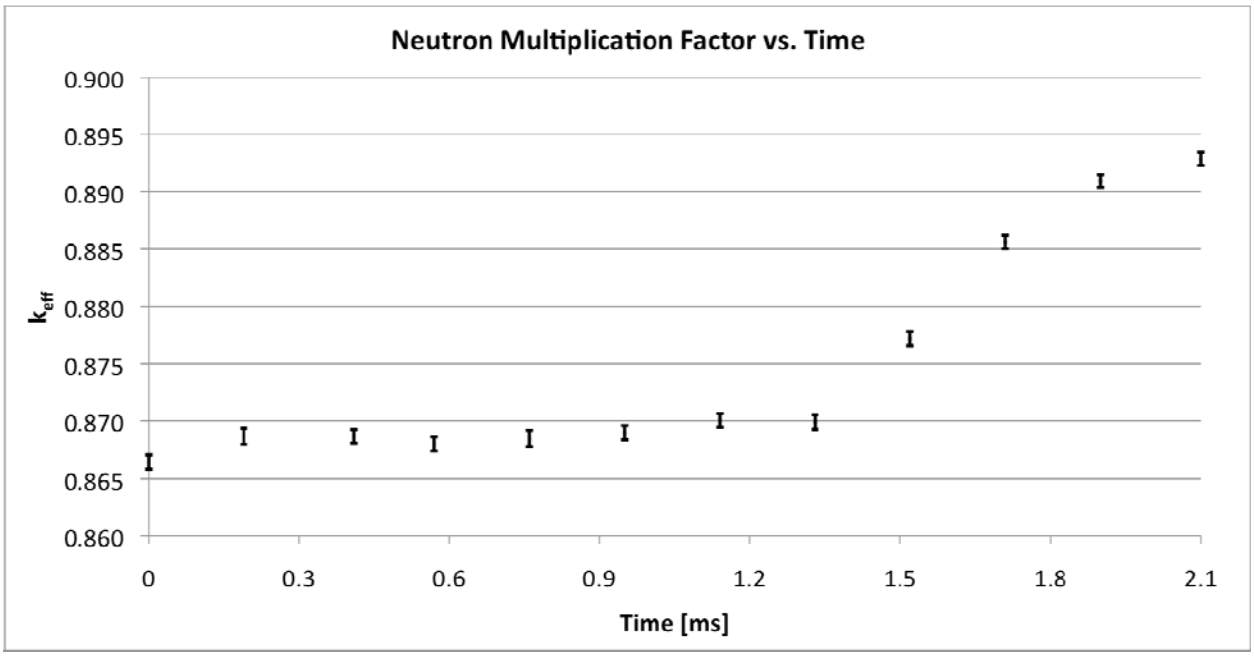

Figure 7-15. Neutron Multiplication Factor during 45-Degree Impact.

7.5. Future Work

Several challenges remain such as modeling fluids, reducing the lost particle fraction, and simplifying the workflow. Fluids are difficult to implicitly model because their enclosing structure can puncture during deformation. Punctures allow mixing between fluids, such as NaK coolant, water shield, and outside air. The current DAGMC methodology allows a single material to be assigned to all fluid space. Although coolant can be explicitly modeled in the structural analysis using hexahedral elements, they quickly become too deformed.

SPH elements have been used successfully to simulate fluids in the structural analysis, as demonstrated in the 0-degree collision. If certain physics conditions are met, spheres may prove acceptable for radiation transport. Although adding spherical elements to MOAB is possible, new methods will need to be developed for efficient ray casting. As currently implemented, all surfaces including spheres are faceted for ray casting. This process will become inefficient if millions of spheres are faceted into many millions of triangles. A better solution may be to determine ray-sphere intersections analytically. MOAB's OBB trees can be constructed with spheres instead of triangles, leaving the current logic intact.

One cause of lost particles is intersecting triangles created when converting quadrilateral mesh faces into triangles. Currently the heuristic splits quadrilaterals into triangles using the shortest diagonal. This is an open research question. Other causes of lost particles need to be analyzed to determine failure mechanisms. Improvements in the transport algorithm are mutually beneficial to deformed mesh and imperfect CAD geometries.

The workflow assumes that models are meshed in Cubit to ensure correspondence between solid and mesh entities. This does not represent a burden for models of medium complexity. However, for models of high complexity meshing occurs in subassemblies that are combined into a composite mesh outside of Cubit. A future DAGMC initialization routine that depends

only upon the deformed mesh and boundary conditions specified inside a separate solid model would simplify the workflow.

8. SUMMARY AND CONCLUSIONS

Techniques for determining impact deformation and the subsequent reactivity change for a space reactor impacting the ground following a potential launch accident have been developed. This technique could be used to determine the margin of subcriticality for such potential accidents. Specifically, the approach couples a finite element continuum mechanics model (Pronto3D or Presto) with a neutronics code (MCNP). DAGMC, developed at the University of Wisconsin-Madison, has been further developed to enable it to handle the distortion following an impact of a reactor onto a hard surface. Improvements have been made to enable MCNP geometric queries to be performed using Pronto3D output.

A sample 85-pin space reactor has been used as a test case for the development process. Presto has been run for this reactor impacting at 100 m/s onto concrete at 0 degrees (cylindrical axis parallel to the velocity vector at impact) and 45 degrees. For the 0 degree case two options were run: one without fluids and one with fluids (NaK coolant in the core and water in the surrounding shield). Without the coolant present, the 0 degree impact resulted in the bottom half of each fuel bin bulging until it touched its neighbor. Considerably less distortion of the core was observed with the fluids present.

DAGMC was used to model the time-dependent reactivity during the impact process. Such an achievement would not have been possible without the extensive modifications and improvements to DAGMC to overcome ray-tracing difficulties created as elements moved, overlapped and died (i.e. removed after a specified amount of distortion occurred). The resulting increase in neutron multiplication factor (and reactivity) was about 7% for the 0 degree impact without fluids and about 2.5% with fluids. For 45 degrees without fluids the increase in neutron multiplication factor was about 2.5%. These numbers are only representative and should not be assumed to be accurate since the fuel material properties assumed in the calculations are not well characterized for large distortions. But the results show the potential for an appreciable reactivity increase due to reactor impact. For the reactor modeled the reactor remained subcritical throughout all impacts (i.e. the neutron multiplication factor, k_{eff}, remained less than 1) because the reactor was designed to have a substantial amount of subcriticality at launch.

9. REFERENCES

Ashcroft, J., and C. Eshelman, “Summary of NR Program Prometheus Efforts,” *Proceedings of the Space Technology and Applications International Forum—STAIF2007*, Albuquerque, NM, February 11, 2007, AIP Conf. Proc., CP880, pp 497-521 (2007).

Attaway, S. W., F.J. Mello, M.W. Heinstein, J.W. Swegle, J.A. Ratner, R.I. Zadoks, *Pronto3d Users’ Instruction: A Transient Dynamic Code for Nonlinear Structural Analysis*, Sandia National Laboratories, SAND98-1361, January 2000a.

Attaway, S. W., RV Matalucci, SW Key, KB Morrill, LJ Malvar, and JE Crawford, *Enhancements to PRONTO3D to Predict Structural Response to Blast*, Sandia National Laboratories Technical Report, SAND2000-1017, May 2000. Export Controlled Information (2000b).

Azom, *www.azom.com* (2010).

Battelle’s Columbus Division, Structural Alloys Handbook, Vol. 2, Columbus OH (1986)

Battelle’s Columbus Division, Structural Alloys Handbook, Vol. 3, Columbus OH (1986)

Blumenthal, W. R., High Strain Rate Compression Testing of Ceramics and Ceramic Composites Los Alamos National Laboratory, American Ceramic Society Copyright.

Bohn, J. H., and M. J. Wozny. A Topology-Based Approach for Shell Closure. Geometric Modeling for Product Realization, pages 297–319 (1993).

Bourne, N. K., *Shock-Induced Failure of Boron Carbide* Proc. R. Soc. Lond. A, 458, pages 1999-2006, The Royal Society (2002).

Brannon, R. M., and S Leelavanichkul, *Survey of Four Damage Models for Concrete*, Sandia National Laboratories Technical Report, SAND2009-5544, August 2009.

Breismeister, J. F, "MCNP A General Neutron Particle Transport Code Version 4B," UC705 and UC700, LA-12625-M, *Version 4B Manual* (March 1997).

Caracappa, P. F., X.G. Xu, “Methods of Integrating Computer Aided Design For Monte Carlo Simulations”, *The Monte Carlo Method: Versatility Unbounded in a Dynamic Computing World*, Chattanooga, TN, April 17-21, 2005.

Clark, B. W., *Cubit: geometry and mesh generation toolkit*, Sandia National Laboratories Report, SAND2008-6533C (2008).

Dewar, J. A., *To the End of the Solar System, The Story of the Nuclear Rocket*, Second Edition, Apogee Books, Collector’s Guide Publishing, Inc., Burlington, Ontario, Canada, pp. 110, 179-184 (2007).

Elliott, J. O., R. J. Lipinski and D. I. Poston, ”Mission Concept for a Nuclear Reactor-Powered Mars Cryobot Lander,” *Proceedings of the Space Technology and Applications International Forum—STAIF2003*, Albuquerque, NM, February 2-5, 2003, AIP Conf. Proc., CP654, pp 353-360 (2003).

Evans, A. G., *The strength and fracture of UO_2*, Journal of nuclear materials (1969).

French, A. P., *Newtonian Mechanics (The M.I.T. Introductory Physics Series), 1st ed.,* p 210, W. W. Norton & Company Inc., New York, NY (1971).

Goods, S. H., and D. E. Dombrowski *Mechanical Properties of S-65C Grade Beryllium at Elevated Temperatures*, Sandia National Laboratories Technical Report, SAND-98-8400 (1998).

Gwinn, K. W., and K. E. Metzinger, “Analysis of Foam Impact onto the Columbia Shuttle Wing Leading Edge Panels using Pronto3D/SPH”, *42nd AIAA Aerospace Sciences Meeting and Exhibit, Jan 5-8, 2004, Reno, NV*, AIAA 2004-942 (2004).

Horn, W. P., and D. L. Taylor. A Theorem to Determine the Spatial Containment of a Point in a Planar Polyhedron. Computer Vision, Graphics, and Image Processing, 45:106–116 (1988).

Khamayseh, A., and A. Kuprat. Deterministic Point Inclusion Methods for Computational Applications with Complex Geometry. Computational Science and Discovery, 1, 2008.

King, J. C., and M. S. El-Genk, “A Methodology for the Neutronics Design of Space Nuclear Reactors,” *Proceedings of the Space Technology and Applications International Forum—STAIF2004*, Albuquerque, NM, February 8-11, 2004, AIP Conf. Proc., CP699, pp 319-329 (2004).

King, J. C., and M. S. El-Genk, “Spectral Shift Absorbers for Fast Spectrum Space Nuclear Reactors,” *Proceedings of the Space Technology and Applications International Forum—STAIF2005*, Albuquerque, NM, February 10-14, 2005, AIP Conf. Proc., CP746, pp 285-294 (2005).

Klein, M., “Nuclear Thermal Rocket – An Established Space Propulsion Technology,” *Proceedings of the Space Technology and Applications International Forum—STAIF2004*, Albuquerque, NM, February 8-11, 2004, AIP Conf. Proc., CP699, pp 413-419 (2004).

Kutty, T. R. G., K. N. Chandrasekharan, J. P. Panakkal, J. K. Ghosh, *Fracture toughness and fracture energy of sintered uranium dioxide fuel pellets* Journal of Materials Science Letters 6, 260-262 (1987).

Lane, J., B. Magedson, and M. Rarick. An Efficient Point in Polyhedron Algorithm. Computer Vision, Graphics, and Image Processing, 26:118–125 (1984).

Ledbetter, H. M., J. of Applied Physics, v52 no. 3, March (1981).

Lee, S. S., U-S. Min, B. Ahn and S.H. Yoo, J. Materials Science, v33, p687 (1998).

Lipinski, R. J., S. A. Wright, M. P. Sherman, R. X. Lenard, R. A. Talandis, D. I. Poston, R. Kapernick, R. Guffee, R. Reid, J. Elson and J. Lee, "Small Fission Power Systems for Mars," *Proceedings of the Space Technology and Applications International Forum—STAIF2002*, Albuquerque, NM, February 3-6, 2002, AIP Conf. Proc., CP608, pp 1043-1053 (2002).

Malvar, L. J., JE Crawford, JW Wesevich, and D Simons, *A Plasticity Concrete Material Model For Dyna3d*, International Journal of Impact Engineering, Volume 19, Nos 9-10, pp. 847-873 (1997).

Marcille, T. F, D. D. Dixon, G. A. Fischer, S. P. Doherty, D. I. Poston and R. J. Kapernick, "Design of a Low Power, Fast-Spectrum, Liquid-Metal Cooled Surface Reactor System," *Proceedings of the Space Technology and Applications International Forum—STAIF2006*, Albuquerque, NM, February 12-16, 2006, AIP Conf. Proc., CP813, pp 319-326 (2006).

Marder, J. M., *Beryllium in Stress Critical Environments*, Journal of materials Engineering, June 1986 Volume 811 (1986).

Matweb, *www.matweb.com* (2010).

Michel, D. J., J. Moteff and A.J. Lovell, Acta Metallurgica, v21, p1269 (1973).

Nordbeck, S., and B. Rydstedt. Computer Cartography Point-In-Polygon Programs. BIT Numerical Mathematics, 7:39–64 (1967).

Parma, E. J., R. M. Bass, G.. S. Hoovler, E. C. Selcow and R. J. Cerbone, "A Critical Assembly Designed to Measure Neutronic Benchmarks in Support of the Space Nuclear Thermal Propulsion Program," *Proceedings of the Tenth Symposium on Space Nuclear Power Systems*, Albuquerque, NM, January 16. 1993, AIP Conf. Proc, CONF 930103, pp. 785-793 (1993).

Phani, K. K., SK Niyogi, Porosity dependence of ultrasonic velocity and elastic modulus in sintered uranium dioxide – a discussion Journal of Materials Science Letters 5, 427-430 (1986).

Poston, D. I., R. J. Kapernick, D. D. Dixon, B. W. Amiri, T. F. Marcille, "Reference Reactor Module for the Affordable Fission Surface Power System," *Proceedings of the Space Technology and Applications International Forum—STAIF2008*, Albuquerque, NM, February 10-14, 2008, AIP Conf. Proc., CP969, pp 277-284 (2008).

Poston, D. I., R. Kapernick, D. Dixon, J. Werner, L. Qualls and R. Radel, "Reference Reactor Module Design for NASA's Lunar Fission Surface Power System", *Proc. of Nuclear and Emerging Technologies for Space 2009 (NETS-2009), Atlanta, GA, June 14-19, 2009.*

Radel, T. E., R. F. Radel, J. A. Smith, R. J. Lipinski, and P. P. H. Wilson, "Methods for Modeling Impact-Induced Reactivity Changes in Space Reactors," *Proceedings of the Nuclear and Emerging Technologies for Space—NETS2009*, Atlanta, GA, June 14-19 (2009).

Raytheon Corp., http://www.raytheon.com (2010).

Sandia National Laboratories, CUBIT Geometry and Mesh Generation Toolkit, 3 August 2010, http://cubit.sandia.gov (2010).

Sato, S., "CAD/MCNP interface", ITER Neutronics Meeting, Madison, July 24-26, 2006 (2006).

Sawan, M. E., P. P. H. Wilson, T. Tautges, L. El-Guebaly, D. Henderson, T. Bohm, B. Kiedrowski, A. Ibrahim, B. Smith, R. Slaybaugh, "Direct Coupling of 3-D Neutronics with CAD Models Applied to Fusion Systems," *18th Topical Meeting on the Technology of Fusion Energy—TOFE-2008*, San Francisco, CA, September 28-October 2, 2008.

Schoof, L. A., and V. R. Yarberry, "EXODUS II: A Finite Element Data Model," Technical Report SAND92- 2137, Sandia National Laboratories, Albuquerque NM, (1994).

Schwarz, R.A., A.L.. Schwarz, and L. L. Carter, " Conversion Of Computer Aided Design (CAD) Output Files To Monte Carlo N-Particle (MCNP) Input Files", *The Monte Carlo Method: Versatility Unbounded in a Dynamic Computing World*, Chattanooga, TN, April 17-21, 2005.

Shackelford, J. F., and W. Alexander, Materials Science and Engineering Handbook: Chapter 6 "Mechanical Properties of Materials", Boca Raton: CRC Press LLC (2001).

Sierra Solid Mechanics Team, *Presto 4.16 User's Guide*, Sandia National Laboratories Report, SAND2010-3112, Printed May 2010.

Sjaardema, G. D., *Sandia Engineering Analysis Code Access Systems (SEACAS)*, Sandia National Laboratories Report, SAND98-2333, Printed September 1998.

SSINA, Designer Handbook, Specialty Steel Industry of North America, Washington DC (1998).

Swegle, J. W., S. W. Attaway, M. W. Heinstein, FJ Mello, DL Hicks, *An Analysis of Smoothed Particle Hydrodynamics*, Sandia National Laboratories Report, SAND93-2513, Printed March 1994.

Swegle, J., S. W. Attaway, M. W. Heinstein, F. J. Mello and D. L. Hicks, *An Analysis of Smoothed Particle Hydrodynamics*, Sandia National Laboratories, SAND93-2513, March 1994.

Tan, P., B. Lee, and C. Tsangalis, FEA modeling prediction of the transmitted overpressure and particle acceleration within a frame subject to shock tube blast loadings, 18th World IMACS/MODSIM Congress, Cairns, Australia 13-17 July 2009. http://mssanz.org.au/modsim09 (2010).

Tautges, T. J., P. P. H. Wilson, J. A. Kraftcheck, B. M. Smith, and D. L. Henderson, "Acceleration Techniques for Direct Use of CAD-Based Geometries in Monte Carlo Radiation Transport." *Proceedings of the International Conference on Mathematics, Computational Methods, and Reactor Physics*, Saratoga Springs, NY, May 3-7, 2009.

Tautges, T. J., "The Common Geometry Module (CGM): a Generic, Extensible Geometry Interface." *Engineering with Computers*, 17(3):299–314, 2001.

Tautges, T. J., P. P. H. Wilson, J. A. Kraftcheck, B. M. Smith, and D. L. Henderson, "Acceleration Techniques for Direct Use of CAD-Based Geometries in Monte Carlo Radiation Transport." *Proceedings of the International Conference on Mathematics, Computational Methods, and Reactor Physics*, Saratoga Springs, NY, May 3-7, 2009.

Tautges, T. J., R. Meyers, K. Merkley, C. Stimpson, and C. Ernst, "MOAB: A Mesh-Oriented Database," Technical Report SAND2004-1592, Sandia National Laboratories, Albuquerque, NM (2004).

Truscello, V, C., and L. L. Rutger, "The SP-100 Power System," *Proceedings of the 9th Symposium on Space Nuclear Power Systems*, Albuquerque, NM, January 15, 1992, CONF 920104, AIP CP246, Issue 1 (1992).

Tsige-Tamirat, H., and U. Fischer, "CAD Interface For Monte Carlo Particle Codes", The Monte Carlo Method: Versatility Unbounded in a Dynamic Computing World Chattancoga, Tennessee, April 17- 21, 2005.

Villa, D. L., T. N. Tallman and J. A. Smith, *Structural Modeling to Support Deformed Nuclear Reactivity Assessments*, SAND2010-xxxx, Sandia National Laboratories, Albuquerque, NM (2010).

Wang, M., D. L. Henderson, T. J. Tautges, L. El-Guebaly, "Three-Dimensional Modeling of Complex Fusion Devices Using CADMCNPX Interface", *Proceedings 16th ANS Topical Meeting on Fusion Energy, Fusion Science and Technology 47 (4)*, May 2005, pp. 1079-1083 (2005).

White Rock Science, Moritz Geometry Tool, http://www.whiterockscience.com/ (2010).

Wikipedia, Uranium Dioxide, http://en.wikipedia.org/wiki/Uranium_dioxide (2010).

Wilson, R. F., H. M. Dieckamp and D. J. Cockeram, "SNAP 10A Design, Development, and Flight Test," AIAA Second Annual Meeting, San Francisco, CA, July 26-29, 1965, AIAA Paper No. 65-467 (1965).

Wu, Y., and X. G. Xu, "The Need for Further Development of CAD/MCNP Interface Codes," *Computational Medical Physics Radiation Modeling*, pp. 392-394 (2007).

Yi-can, W., L. Ying , L. Lei, Ding Ai-Ping et, "Research and development of the automatic modeling system for Monte Carlo particle transport simulation", *Chinese J. of Nucl. Sci. Eng.*,Vol.26 No.1 20-27.

Distribution

EXTERNAL

Brandon Smith (3)
University of Wisconsin
428 Engineering Research Building
1500 Engineering Dr
Madison, WI 53706
U. of Wisconsin, Madison, WI 53706

Prof. Paul P. H. Wilson (3)
University of Wisconsin
419 Engineering Research Building
1500 Engineering Dr
Madison, WI 53706
U. of Wisconsin, Madison, WI 53706

Tyler N. Tallman (3)
11085 45th Avenue
Chippewa Falls, WI 54729

Lyle Rutger (3)
Department of Energy
DOE/NE-34
19901 Germantown Road
Germantown, MD 20874-1290

Ryan Bechtel (2)
Department of Energy
DOE/NE-34
19901 Germantown Road
Germantown, MD 20874-1290

Bart Bartram
Tetra Tech NUS, Inc.
20251 Century Boulevard, Suite 200
Germantown, MD 20874

Meera Mukunda
Orbital Sciences Corporation
20030 Century Boulevard,Suite 102
Germantown, MD 20874

Yale Chang
John Hopkins University
Applied Research Laboratory (1E-255)
11100 John Hopkins Rd
Laurel MD 20723

INTERNAL

1	MS 0899	Technical Library, 9536 (electronic copy)
1	MS0359	D. Chavez, LDRD Office, 1911

1	MS 0372	J. Redmond, 1525
5	MS 0372	J.A. Smith, 1525
5	MS 0744	D. L. Villa, 6763
1	MS 0736	J.E. Kelly, 6770
1	MS 0736	D.A. Powers, 6770
1	MS 1136	R.F. Radel, 6771
5	MS 0747	R.L. Lipinski, 6774
1	MS 0747	K.B. Sorenson, 6774

Sandia National Laboratories